SECONDARY PROMPT GAMMA RAYS TO IMPROVE PROTON RANGE VERIFICATION

A Thesis
Presented to
The Academic Faculty

by

Jessica Saunders

In Partial Fulfillment
of the Requirements for the Degree
Doctor of Philosophy in the
Nuclear & Radiological Engineering Program

Georgia Institute of Technology
May 2016

SECONDARY PROMPT GAMMA RAYS TO IMPROVE PROTON RANGE VERIFICATION

Approved by:

Dr. Anna Erickson, Committee Chair
School of Mechanical Engineering
Nuclear and Radiological Engineering
Program
Georgia Institute of Technology

Dr. Anna Erickson, Advisor
School of Mechanical Engineering
Nuclear and Radiological Engineering
Program
Georgia Institute of Technology

Dr. Eric Elder
School of Mechanical Engineering
Nuclear and Radiological Engineering
Program
Georgia Institute of Technology

Dr. Nolan Hertel
School of Mechanical Engineering
Nuclear and Radiological Engineering
Program
Georgia Institute of Technology

Dr. Farzad Rahnema
School of Mechanical Engineering
Nuclear and Radiological Engineering
Program
Georgia Institute of Technology

Dr. Justin Roper
Winship Cancer Institute
Department of Radiation Oncology
Emory University

Date Approved: 22 March 2016

ACKNOWLEDGEMENTS

TABLE OF CONTENTS

LIST OF TABLES

LIST OF FIGURES

LIST OF SYMBOLS AND ABBREVIATIONS

Gy	Gray
kV	Kilovolt
MV	Megavolt
2D	Two dimensional
3D	Three dimensional
eV	Electron-volts
keV	Kiloelectron-volts
MeV	Megaelectron-volts
mm	Millimeter
cm	Centimeter
I-value	Mean ionization energy
ft	Feet
in	Inch
E_b	Binding energy
E_{pe}	Energy of photoelectron
λ	Gamma-ray energy
OAR	Organ(s) at risk
LET	Linear energy transfer
RSP	Relative stopping power
PG	Prompt gamma-rays
CT	Computer tomography
pCT	Proton computer tomography
HU	Hounsfield Unit
PET	Positron emission tomography
MRI	Magnetic resonance imaging
MCS	Multiple Coulomb scattering
MC	Monte Carlo
MU	Monitor Unit
SPECT	Single photon emission tomography
SOBP	Spread-Out Bragg-Peak
TOF	Time-of-flight
ICRU	International Commission on Radiation Units & Measurements
PMMA	Poly(methyl methacrylate)
HDPE	High-density polyethylene
LANL	Los Alamos National Laboratory
MCNP	Monte Carlo nuclear transport code
SRIM	Stopping and Range of Ions in Matter
CPC	Northwestern Medicine Chicago Proton Center
$LaBr_3$:Ce	Cerium-doped lanthanum(III) bromide
PMT	Photomultiplier tube
NNDC	National Nuclear Data Center

SUMMARY

The goal of this research is to evaluate the secondary prompt gamma (PG) yield from proton therapy at high characteristic energies from MC model simulations and experimental data. Recent studies indicate that target composition influences PG characteristic energy and yield, and the quantification of PG may be used to offer real-time dose verification for proton therapy. In this study PG analysis was performed for MC simulations to evaluate the characteristic measurements and total yield of secondary PG emitted from a target in the 0-8 MeV range from a proton therapy beam over a range of four different beam energies (70 MeV, 160 MeV, 200 MeV, 220 MeV). This was repeated in several target materials (carbon, calcium oxide, calcium fluoride, PMMA, and HDPE) in order to evaluate the influence of the incident energy and the target material on the PG yield and energy spectra. PG energy spectra determined from the specified target materials indicated that the 3.74 MeV energy peak shows a linear correlation between PG intensity and calcium mass fraction of the target material. 6.13 MeV and 4.44 MeV energy peak are not unique to the respective, oxygen and combined oxygen and carbon, mass fraction of the target material. This relationship is complicated by the addition of calcium within the target. Experimental data was collected in order to validate the computational model based on comparison of relative characteristic energy peek intensities. The relative peak ratio determined from experimental data is in good agreement with model prediction, the combined peak ratio is within 0.2%.

CHAPTER I

INTRODUCTION

1.1 Background

The overarching goal of any external beam radiation treatment therapy is to administer a uniform dose to precisely targeted tissue while minimizing dose to healthy tissue and to organs at risk (OAR). Any recent and future improvements in accuracy and dose delivery generally come from improved contouring of the target region [12]. Traditionally, high-energy photon and electron beams have been the predominant sources used for medical ionizing radiation treatment applications due to their well characterized gradual dose fall off. However, the depth dose curves for both of these particle types peak at or near the surface of the exposed tissue, limiting their effectiveness for treating tissue deeper within the patient, as seen in Fig. 1. Recent advances in technology have created renewed interest in proton therapy for medical applications.

While knowledge of the potential advantages for proton therapy due to the unique interaction characteristics of protons has been available for several decades, it has not been capitalized on in clinical applications primarily due to the large capital expense, the particle range uncertainty, and long reconstruction computing times [12]. Dedicated multi-room treatment facilities and continued advancements in computing power have allowed us to work through the capital expense and computing time limitations. As a result, this has created a renewed interest and need for improved range verification in order to improve treatment planning and dosimetry for proton therapy. There are currently a variety of methods of proton range verification being investigated, including direct measurements, calculations based on indirect measurements, as well as improved reconstruction algorithms [12].
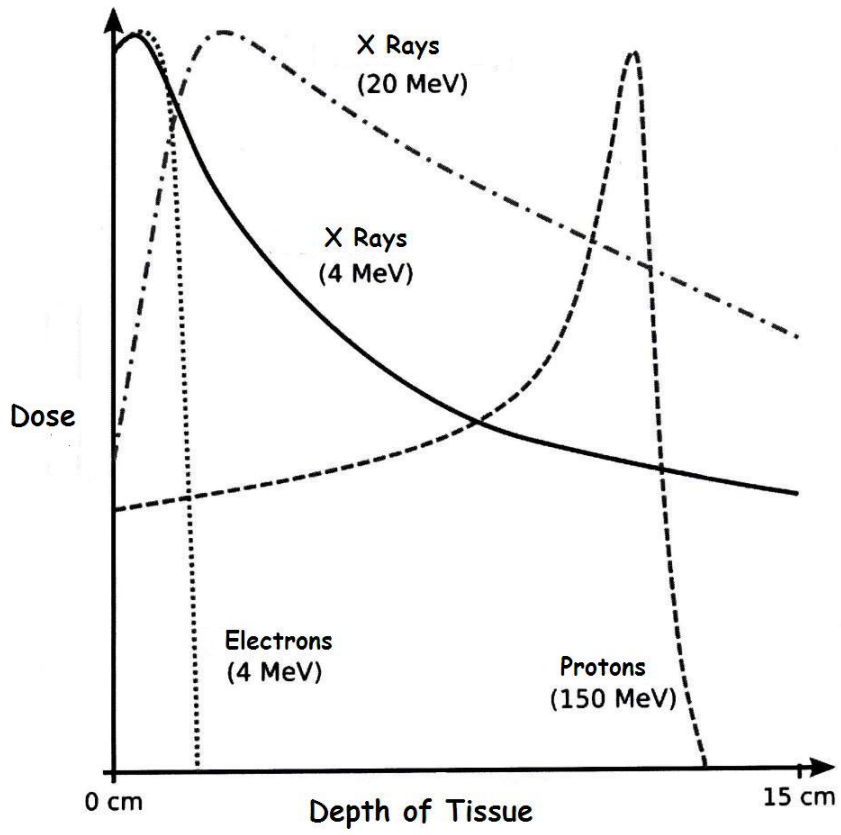
Figure 1: Depth Dose Curve: comparison of the depth dose profiles for various particle beams, (a) 4 MeV electron beam (b) 4 MeV photon beam, (c) 20 MeV photon beam and (d) 150 MeV proton beam.[8]

Table 1: Research Questions.

1. What is the absolute yield of secondary PG from a proton beam at clinically relevant energies of 70, 160, 200, and 220?

2. Can target material or the RSP be determined based on the absolute yield of the secondary PG from a proton beam?

3. Can location specific energy spectra of the secondary PG from a proton beam be used to determine target material or the RSP along the proton path?

1.2 Objective

This research will evaluate the secondary prompt gamma (PG) yield resulting from target interactions with proton beams at high characteristic energies used in proton therapy based on Monte Carlo (MC) model simulations. Recent studies indicate that target composition influences PG characteristic energy and yield, and the quantification of PG may be used to offer real-time dose and range verification for proton therapy. To evaluate this, a computational model was developed to generate the predicted secondary PGs resulting from proton beam interactions at four clinically relevant energies (70 MeV, 160 MeV, 200 MeV, and 220 MeV), in several target materials (carbon, calcium fluorine, calcium oxide, PMMA, and HDPE) are compared in order to evaluate the influence of the incident energy and the target material on the PG energy spectra. The total yield of secondary PGs emitted and the characteristic energy PGs released from interactions of a proton therapy beam with a target are determined and evaluated for correlations with range and material composition, respectively.

In order to benchmark our MCNP simulation results, experimental measurements of the PG emitted from a target composed of carbon, oxygen and hydrogen are taken and the resulting PG energy spectra ratios are compared to those produced by the MCNP simulations. Specifically, the experimental data collected from Chicago Proton Center (CPC) is analyzed to evaluate the location specific, characteristic energy spectra for each of the targets. These results are then compared with the respective results generated by the MCNP code package. Finally the uncertainty of the calculations are evaluated.

1.3 Current Technologies and Methods in Proton Therapy

1.3.1 Proton Therapy: Method

Proton therapy uses heavy charged particles to irradiate unhealthy tissue. Recently, this method has gained popularity as it looks to take advantage of the lower integral dose to the patient, the well-defined range, and sharp dose fall-off characteristic of heavy charged particle interactions, as shown in Fig. 1 by the proton curve. In contrast to photon and electron beams, proton beams deliver a relatively constant and minimal dose to the surface and superficial tissue, depositing the majority of their dose near the incident particles end of range. The velocity of the proton particle is much higher near the surface of the target object than in the deeper regions. Based on the Bethe-Bloch formula, which will be discussed further on, the energy deposited per unit length is inversely proportional to the square of the particle velocity. Thus the proton particles deposit most of the dose in the Bragg peak region just before reaching their end of range [21]. Relatively no dose is distributed to tissue beyond the peak depth or distal-edge of the Bragg peak, allowing the Bragg peak to be placed directly over a target region by adjusting the energy of the incident proton beam. Because the Bragg peak is most often smaller than the tumor or treatment region, what is known as a spread-out Bragg peak (SOBP) is used. While this is executed in various ways it is effectively the delivery of a series of incident beam energies in various time increments in order to cover the area of interest as displayed in Fig. 2.

An ideal proton treatment plan would align the Bragg peak with the target tissue, and the distal-edge of the Bragg peak could be placed immediately in front of healthy tissue or OAR, as described in the top image of Fig. 3. Unfortunately, this is not current practice due to the range uncertainty and the dramatic change in delivered dose resulting from minimal changes to proton range, as depicted by the lower images in Fig. 3. Uncertainties in the exact position of the Bragg peak result from a combination of organ motion, setup and anatomical variations, dose calculation approximations and biological considerations [20]. Accurate proton treatment planning requires the use of the tissues relative stopping power (RSP), which is the mean energy loss of protons per unit path length of the material
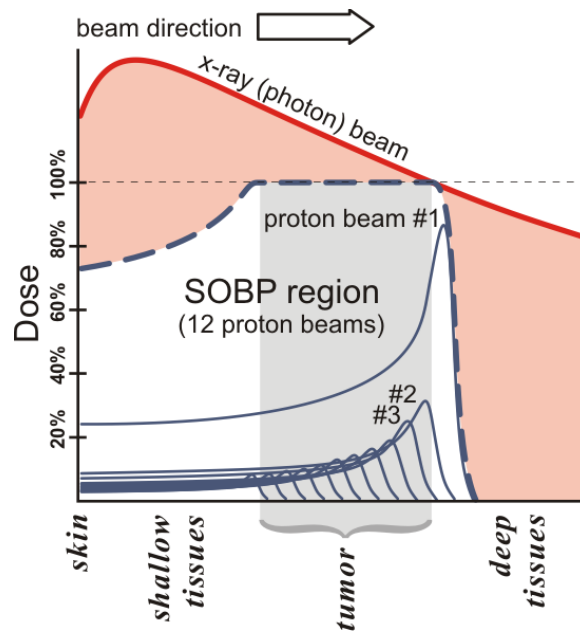
Figure 2: Spread out Bragg peak: The SOBP is the summation of a series of individual Bragg peaks generated over various energies [15].
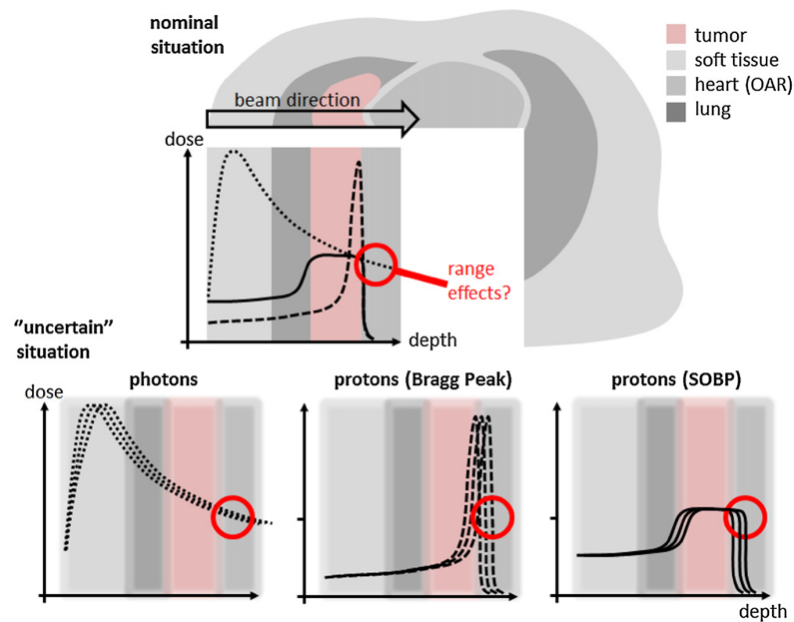
Figure 3: This image depicts the dose delivery benefits of proton irradiation relative to photon irradiation. It also highlights the increased importance of range accuracy from proton treatment due to the abrupt changes to delivered dose that occur with minute changes in range. Image as seen in [12].

relative to that of water. This is because the proton interactions are dependent on Coulomb interactions in addition to being affected by the chemical composition of the materials and their electron density.

1.3.2 Proton Therapy: Imaging

Treatment planning, patient setup, and anatomical localization for proton therapy depend on some form of imaging to provide various pieces of patient specific data. One of the notable limitations of proton beam planning is the range uncertainty of approximately 1-2%, which is particularly significant for proton treatments since small variations dramatically alter deposited dose to tissue regions at the distal end of the range. This can be visualized by comparing the change in delivered dose due to a shift in range for photons versus protons as shown in the lower three images of Fig. 3.

1.3.2.1 Current Imaging Method

The currently accepted method for proton treatment planning is very similar to that of photon therapy. A photon computer tomography (CT) of the patient is obtained to provide patient specific anatomical localization and the tissues photon attenuation information. This is determined from the images based on Hounsfield Unit (HU) values, which are a measure of the tissues contrast relative to that of water. The HU values are then converted to RSP, and the tumor(s) and OAR are contoured on the collected images. This information is then used to determine the treatment factors such as the beam configurations, the aperture and compensators, and the beam weightings, satisfying a specific set of dose-volume constraints. Next the output factor measurements for each field are taken as a quality assurance step. Then, on the day of treatment delivery, patient setup is verified with x-ray image guidance, and dose is delivered. There is currently no direct range verification or feedback loop as used with photon and electron therapy due to their relatively linear fall off or exit dose.

The limited accuracy due to x-ray CT treatment planning for proton therapy is, in part, due to differences in the interactions of x-rays and heavy charged particles. HU values are based on photon attenuation, which is dependent on electron density. In contrast RSP

6

values depend on the chemical composition of the tissue(s) and Coulomb interactions. In order to convert the HU values to RSP, a conversion factor is determined based either on empirical data collected from the simulation CT scanner for various tissues or according to a stoichiometric calibration method designed to reduce the error due to nonhuman tissue phantoms [30]. This calibration curve is determined based on theoretical HU values and RSPs determined from assumed atomic compositions of tissues determined by experimental measurements on tissue equivalent materials. This is currently the most predominantly used method [30].

The HU values are not unique for each RSP because these two values are describing two corresponding but different physical properties [30]. In addition, HU values are affected by beam hardening and tissue location in the beam whereas RSP values are not. This conversion step can contribute to the overall range uncertainty (up to 2%) [12]. Ultimately, any method of determining RSP from HU numbers is handicapped due to the degeneracy in correlation between HU and RSP of various materials. The removal or a reduced dependency on this conversion factor could improve treatment accuracy by reducing range uncertainty.

1.3.2.2   Current Experimental Imaging Method

There are currently a variety of methods of proton range verification being investigated. These include both direct measurements, such as point dose, range probe, and proton radiography/tomography; calculations based on indirect measurements, such as PG imaging, positron emission tomography (PET) imaging, magnetic resonance imaging (MRI) imaging, and hybrid imaging systems as well as improved reconstruction algorithms [12]. A closer review of several of these methods will be described in the following sections.

One method for reducing the proton range uncertainty is to remove the conversion from HU value to RSP [22]. The RSP could be determined directly by generating images with a proton source, such as with proton computer tomography (pCT). During a pCT scan a low intensity beam of high-energy protons is used to generate radiographic (2D) or tomographic (3D) images. As protons travel though matter they lose energy though inelastic

collisions, resulting in ionizations and excitations, and elastic collisions that result in small-angle deflections of the incident protons called Multiple Coulomb Scattering (MCS). Due to the relatively large number of interactions that take place over the path-length, significant deviation from the protons original direction is observed. As these interactions take place at random, a statistical distribution results in both the amount of energy lost by the incident particle per interaction and the lateral and angular change from the incident direction [27]. Because of the MCS, it is not possible to track the trajectory and path length of the proton directly, but there are several methods suggested to reconstruct the particle's path.

A pCT imaging device is composed of (a) two parallel tracking plates, in front of and behind the object, that measure the entrance and exit position (location) and direction (angle) of the particles and (b) a calorimeter which measures the exit energy. Fig. 4 depicts a current proton CT system [7]. This proton transmission information allows for the reconstruction of the energy loss of the incident proton or the density distribution of the traversed tissue leading to the calculation of the averaged RSP of the track length. This information can be used directly as input for proton radiotherapy treatment planning [26]. According to Schulte [27], the use of pCT could reduce proton therapy range uncertainty due to the relative electron densities of the tissues. Further, it could remove the uncertainty from the acquisition of HU values and the inaccuracies due to artifacts with proton doses comparable to those of x-ray or cone beam CT.

Another method of reducing uncertainty currently being investigated is indirect proton range measurement which can be determined through the detection of the resulting gamma-rays. The two methods currently under investigation are PET imaging and PG detection. PET imaging, which is the detection of coincident gammas from positron annihilation, can be used to detect the positrons emitted from the isotopes resulting from proton nuclear interactions. Limitations of this method are due to the fact that induced activity is dependent on tissue composition. Calculations are further complicated by activation threshold energies. PET imaging uses gamma cameras to detect photons from pair annihilation of a positron and an electron at the fixed energy of 511 keV with energy collimation. In the case of proton therapy, the positron emitters are produced by nuclear reactions that result
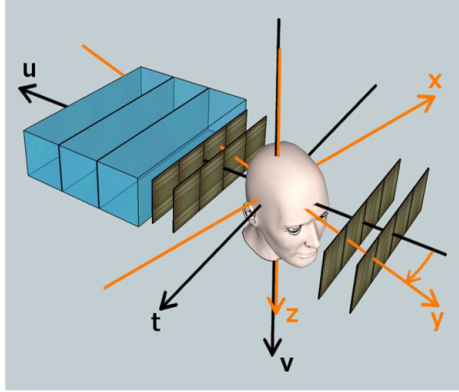
Figure 4: pCT imaging device is composed of (a) two parallel tracking plates, in front of and behind the object, that measure the entrance and exit position (location) and direction (angle) of the particles and (b) a calorimeter which measures the exit energy. Image as seen in [22].

from inelastic collisions between the incident proton and target nucleus [26].In this case the detected annihilation photons produced in the patient can be used to indicate the location of the proton beam within the patient and relate this to their anatomy [29]. The application of PET for real-time monitor is difficult because the decay time of PET isotopes is significantly longer relative to PG emission time and it is not an effective use of clinical therapy treatment rooms [10]. Unfortunately, there is a divergent relationship between the induced activity distribution and the dose distribution due to the dependence on the elemental composition [12].

PGs are the result of nuclei excitation along the proton path. These interactions, which release the PG, with an energy range of 2-15 MeV, occur along the whole of the proton path, stopping a few millimeters before the Bragg peak, approximately within 2-3 mm [12]. This fall off is the result of the drop in reaction cross section due to the decreasing energy of the incident particle [12]. "After an interaction, the target nucleus is excited to a higher energy state and then emits a single photon (prompt gammas) to return to its ground state." [12] While it is important to note that the falloff in PG emission is not equal to
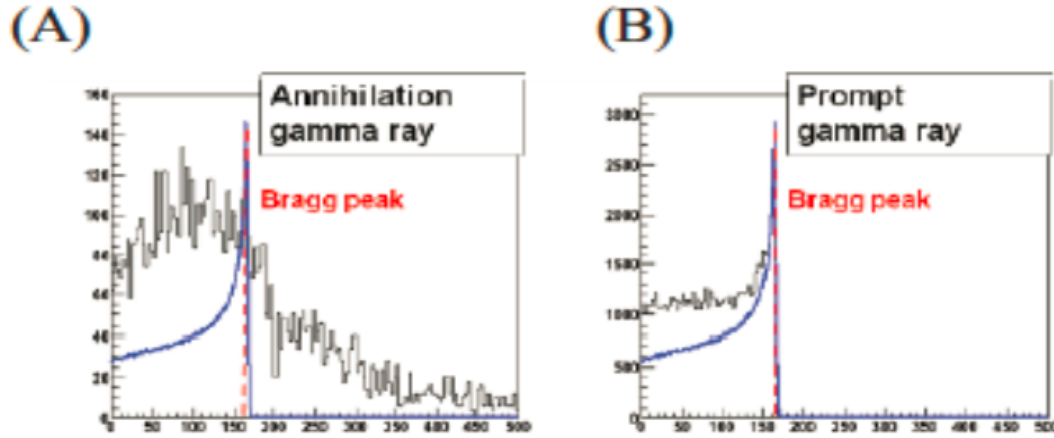
Figure 5: Compares the intensity distribution of (A) annihilation gamma-rays and (B) PGs (shown as solid black line) with the energy deposited by a proton beam (shown in by solid blue line) along the depth of a simulated target in millimeters. Image as seen in [10].

the dose falloff, this method allows real time dose delivery verification. However, clinical application requires enhanced detectors for gamma detection in this energy range because these energies are often too high to be fully deposited in the detector region. "Interestingly, for the latter method [PG], the maximum in the cross section as a function of energy is at lower energies compared to the PET isotope production cross sections. This causes the depth position of the maximum in the photon signal to be closer to the Bragg peak than in the case of the PET imaging method [19]. [See Fig. 5.] Another advantage compared to the PET method is a potentially higher count rate." [20]. As a proton therapy plan is typically delivered at a 2 Gy/min dose rate which yields a proton flux on the order of $5 * 10^9 / cm^2 / g$, the resulting inelastic emission rate per volume is the product of the flux, cross-section, and number density. As an example ^{16}O would result in a rate of $3.5 * 10^{55} / cm^3 / s$.

CHAPTER II

PHYSICS

2.1 Basic Proton Physics in Matter

In order to improve the accuracy of any dose delivery it is useful to have a working knowledge of the proton interaction behavior in matter. Protons are heavy charged particles. They interact with matter through both elastic and inelastic interactions. These interactions result in stopping, scattering, and nuclear reactions.

2.1.1 Stopping

As the protons move though material, they continually lose kinetic energy through interactions with the orbital electrons of the medium until they eventually come to a stop within the medium. This empirical process is best described by the Bethe-Block theory of stopping power, which was developed to describe slowing down and stopping behavior of heavy charged particles, such as protons, as they interact with matter. According to Attix [2], stopping power is the expectation value of the rate of energy loss per unit path length by a particular charged particle of a specific energy in a medium. It is dependent on the initial energy of the particle and the electron density and mean ionization energy of the medium. The incident particle transfers increasing amounts of its kinetic energy as it slows down along the track length, ultimately depositing the majority of its energy near its end of range. For clinical applications the Bethe-Bloch formula can be represented as follows:

$$-\frac{dE}{dx}(r) = \eta_e(r)S(I(r), E(r)) \tag{1}$$

"where η_e is the relative electron density with respect to water, I(r) is the mean excitation potential of the material, which for water is 75 eV, E(r) the proton energy, and S is the proton stopping power in water, which can be expressed as [depicted in Eq. 2]"

$$S(I(r), E(r)) = K\frac{1}{\beta^2(E))}[ln(\frac{(2m_ec^2)}{I(r)}\frac{\beta^2(E)}{1-\beta^2(E)}) - \beta^2(E)] \tag{2}$$

"The constant K is often assumed to be 170 MeV/cm and combines various physical parameters, m_e is the electron mass and is the proton velocity relative to the speed of light. The dependence on the position vector r is a reminder that all quantities in [the stopping power equation] can vary with spatial position in the object." [27] "For tissues, the uncertainty in I-value is potentially on the order of 10 -15% (Andreo 2009). This might result in a range uncertainty in tissue of 1.5%", see Fig. 3 [20].

2.1.2   Scattering

The predominant reaction type is elastic interactions resulting in scattering reactions also known as MCS. In these reactions the incident proton collides with orbital electrons of the medium and transfers a portion of the protons kinetic energy to the electron. This results in the electron being excited or ejected from its orbital and the proton being redirected at a slight angle with an overall forward projection and a slightly lower kinetic energy.

2.1.3   Nuclear Reactions

In addition to the stopping and MCS that results from interactions with orbital electrons, incident protons can also undergo nuclear reactions which are inelastic collisions that interact with and excite the atomic nuclei resulting in an unstable atom. These interactions result in the generation of secondary particles including gamma-rays, neutrons, protons and, more rarely, alpha particles as the atom works to return to a stable configuration. This type of interaction takes place about 15-20% of the time depending on the energy of the particle. These reactions result in the knock off of a nucleon that re-stabilizes through positron emission or excitation which return to ground state by releasing PGs.

PGs are the result of nuclear reactions that result in nuclei excitation along the proton path. These characteristic prompt gammas are released with an energy range of 2-15 MeV depending on the atom from which they were generated. Production of PGs stop several millimeters before the Bragg peak due to the incident particles reduced kinetic energy. Detection and quantification of these PGs allows real time dose delivery verification [12].

2.2 Secondary Measurements: Prompt Gammas

Evaluation of the prompt gamma-rays resulting from proton beam interaction with a target has the potential to not only provide improved online range verification to within 1-2 mm accuracy but also provide additional useful information regarding elemental tissue composition based on the analysis of the PG energy spectra. In addition to range verification, the emitted PG spectrum can be used to determine the elemental composition of tissue along the tack length [24]. According to Yang [30], the most significant factor affecting overall RSP uncertainty is the variations in tissue composition, especially in soft tissue, since it is the dominant tissue type in patients. This suggests the importance of determining the patient specific tissue composition in order to reduce its impact on the overall uncertainties in proton RSP estimation [30]. Yang [30] found "that the key tissue composition factors were the mass density and the percentages of hydrogen (H) and calcium (Ca)." [30] "The emission spectrum is in the range of MeV... The most prominent lines are 511 keV (positron annihilation), 2.2 MeV (deuterium), 4.4 MeV (carbon) and 6.1 MeV (oxygen)." [13] The relative intensity ratios of the peaks of interest could provide additional information for improved RSP calculations as well as "a method for analyzing changes in the tissue composition in vivo during irradiation, or from treatment fraction to treatment fraction." [12]

Proton interactions result in inelastic nuclear reactions that produce gamma rays approximately 15-20 percent of the time for intermediate incident energy ranges (reaction rate approximately 20% at 160MeV [14]). This can result in either PG emitting from excited target nuclei or coincident gammas emitting from positron emission isotopes [[17],[12]]. Coincident detection of gamma-rays would apply PET, thus require longer count acquisition times due to low efficiency and require off-line detection. In contrast, PGs are emitted very quickly after the initial inelastic nuclear reaction, within 10^{-19}-10^{-9} sec, and the lack of coincident collimation permits increased acquisition efficiency, which allows for real-time/live detection [14]. These PGs are emitted at characteristic energy levels, in the MeV range (2-15 MeV), that are unique to the specific atomic nucleus from which they are released. Thus,

the resulting energy spectra can be analyzed to provide additional localized information regarding the atomic fractions of the material the proton travels through. Capturing and incorporating this information would allow for improved treatment planning and monitoring without additional dose delivered to patient [12].

2.3 Prompt Gamma Detection Method

PGs are emitted along the entire proton path up "until 2-3 mm [anterior] to the Bragg-peak", allowing for range verification of the dose deposition in the target material [12]. The resulting spectra are relatively noisy particularly at the tail due to scatter, bremsstrahlung and neutron contamination. In order to understand the challenges associated with detecting PG it is useful to have a general understanding of types of interactions gamma-rays may undergo.

2.3.1 Gamma-ray Interaction

Gamma-rays are packets of energy or photons released from the nucleus of an atom. They can interact with matter in three ways, though photoelectric absorption, Compton scatter, or pair production. The probability of the type of interaction that takes place is governed by the energy of the photon and the atomic number, or Z of the material, with which it interacts. Photoelectric absorption dominates in high Z materials at low energies. As the energy of the gamma increases Compton scatter effect becomes more predominant for all Z materials until roughly 10 MeV. Around this energy pair production takes over for high Z material.

2.3.1.1 Photoelectric Absorption

Photoelectric effect describes the phenomenon in which a gamma-ray interacts with an electron that is tightly bound to an atom. The incident energy of the gamma-ray, λ, must be greater than or equal to the binding energy, E_b, of the electron. During the interaction the gamma-ray disappears and results in the release of a photonelectron from one of the electron shells. The kinetic energy of the photoelectron, E_{pe}, is described by Eq. 3. The
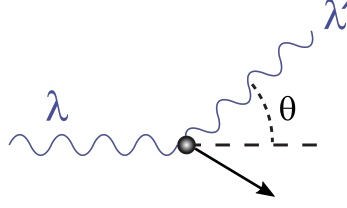
Figure 6: Diagram depicting Compton scattering effect in which the incident gamma-ray, λ, interacts with a free electron. This interaction results in a recoil electron and a scattered photon, λ', which share the energy of incident gamma-ray. Source [9].

binding energy is also released by an Auger electron or as a characteristic X-ray and the vacancy created in the electron shell is filled by rearranging the remaining electrons.

$$E_{pe} = \lambda - E_b \tag{3}$$

2.3.1.2 Compton Scatter

Compton scatter effect describes an elastic collision in which the incident gamma-ray interacts with a free electron. A free electron describes an electron with a binding energy significantly less than the energy of the incident gamma-ray. This interaction results in a recoil electron and a scattered photon which share the energy of incident gamma-ray as shown in Fig. 6 and described by Eq. 4.

$$E_{e^-} = \lambda - \lambda' = \lambda \left(\frac{\frac{(\lambda/m_0 c^2)}{1 - cos(\Theta)}}{1 + \frac{(\lambda/m_0 c^2)}{1 - cos(\Theta)}} \right) \tag{4}$$

As dictated by Eq. 4 there are two limiting cases, when Θ equals 0 or 180 degrees. When Θ equals 0, none of the incident energy is transferred to the electron and the photon continues in the incident direction. However, when Θ equals 180 degrees the maximum amount of energy is transferred to the electron as the gamma-ray is back-scattered. Since all scattering angles can occur, a Compton continuum is observed. The energy of the scattered photon can be determined from Eq. 5. Doppler broadening, due to "finite momentum of orbital electrons, also cause the gamma-rays that are scattered at a fixed angle from" the source to have a narrow energy distribution rather than a single energy as theoretically predicted by Eq. 5. [11]

$$\lambda' \mid_{\Theta=\Pi} = \frac{\lambda}{1 + 2\lambda/m_0c^2} \tag{5}$$

2.3.1.3   Pair Production

Pair production is an inelastic reaction that takes place as an incident gamma-ray, with an incident energy greater than 1.02 MeV, passes though an intense electric field near a nucleus (or electron, though with significantly less probability and a higher threshold energy of $4m_0c^2$). The gamma-ray may spontaneously convert into an electron and a positron, with a combined kinetic energy roughly equal to the incident energy less $2m_0c^2$, roughly 1.02 MeV, as seen in Eq. 6.

$$E_{e^-} + E_{e^+} = \lambda - 2m_0c^2 \tag{6}$$

Since the positron is not stable, once it comes into contact with one of the surrounding electrons it will annihilate, releasing two 511 keV photons. This reaction takes place very quickly and near the initial reaction and thus is perceived to be in coincidence with the initial pair production reaction. For detection purposes, if one or both on the annihilation photons escapes the detector, a peak equal to the incident energy less 0.511 MeV or 1.02 MeV respectively will be observed.

2.3.2   Detectors

Any detector used for this application would need to be able to completely absorb the energy of the incident PG. This is particularly challenging for this application as the energy range of the particles of interest which are between 2-7 MeV, much higher than sweet spot of equipment currently on the market for clinical applications. Much current research is being focused on the effort to build a detector that is optimized for this energy range.

2.3.2.1   Collimated Prompt Gamma Camera

The gamma camera is the same as that used with single-photon emission computed tomography (SPECT) imaging but with improved detectors capable of capturing high energy gamma rays with high resolution energy and efficiency. "In early setups [the collimated

prompt gamma camera] approach was challenged by neutron background radiation and stray gammas, necessitating thick layers of collimation. [MC] simulations imply, however, that array-type setups would allow for the measurement of prompt gamma distributions from therapeutic proton beams" [18]. On the other hand, a recent publication by Bom et al. [4] claims that challenges could be solved by using a gamma camera in combination with a knife-edge shaped slit placed perpendicular to the beam direction. It has also been shown by Biegun et al. [3] and J. Polf [24] that this can be cleaned up by incorporating neutron suppression through time-of-flight (TOF) techniques or Compton suppression. TOF techniques can be used to flag PG that are emitted within a specified time window relative to the release on the incident beam particles. "Compton suppression uses guarded detector to measure the scattered Compton background, which can be subtracted from the primary detector. In MC simulations they show that under common therapy conditions for proton spot scanning, enough data during one spot can be collected to enable identification of the location of the distal dose edge with a 1 sigma accuracy of better than 1 mm." [12] A prototype was successfully tested by Smeets et al. [28] for 100 and 160 MeV energy beams.

CHAPTER III

MONTE CARLO MODEL

3.1   Monte Carlo: MCNP

Los Alamos National Laboratory (LANL) maintains and updates a MC nuclear transport code commonly referred to as MCNP. It is a software package that was designed to simulate nuclear processes [16]. The most recent version, MCNP6, is an update that merges the capabilities of MCNP5 and MCNPX. MCNPX (MCNP extended) was developed to track a larger range of particle types and heavy ions over a wider range of energies making it particularly useful for medical physics studies. The new version "has been expanded to handle a multitude of particles and to include model physics options for energies above the cross-section table range, a material burnup feature, and delayed particle production." [16] It also provides "[e]xpanded and/or new tally, source, and variance-reduction options." [16]

3.2   Preliminary MC Simulation of PG Generation

In the preliminary simulations MCNP6 was used to simulate PG emission spectra generated from proton induced nuclear reactions in medium of varying composition of carbon, oxygen, calcium, and nitrogen, the predominant elements found in human tissue. The relative peak intensities at discrete energies predicted by MCNP6 were compared to the corresponding atomic composition of the medium.
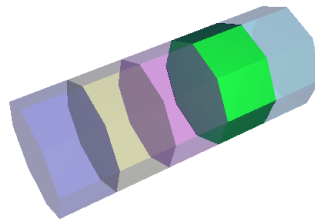
Figure 7: Simulation Phantom: cylindrical phantom (5cm x 2cm (r=1cm)) made up of five 1 cm homogeneous subsections.
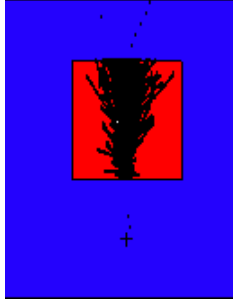
Figure 8: Cross-section of cylindrical phantom (5cm x 2cm (r=1cm)), in red. Black tracks indicate a binary representation of the interaction track of incident proton particles as they move through air and the target material. This neglects the relative intensity of tracks, which, if depicted, would show a greater concentration of tracks tightly packed in the center.

In this simulation model, the incident proton particles are targeted on a cylindrical phantom (5cm x 2cm (r=1cm)) made up of five 1 cm homogeneous subsections, see Fig. 7. The source is 10 cm away from the surface of the target. Both the source and phantom are staged in a "room" (12 x 14 x 9 ft^3) filled with air. This MCNP6 model is tracking the interactions resulting from a mono-energetic proton source that released 10^6 particles at 40 MeV from a disk source, 1 cm radius, uni-directionally in the $+z$ direction. Fig. 8 graphically displays the proton particle tracks as they enter and move through the target. This model neglects any energy straggle or degradation of the 40 MeV protons due to generation or interaction with the beam nozzle as they are released and any interactions structural or stabilization equipment (e.g. couch) that would potentially interfere.

As output, energy spectra are generated from the PGs that originate from within and escape the specified cell of interest of the phantom: the solid green cell depicted in the phantom, Fig. 7. Fig. 8 shows a cross-section of cylindrical phantom. The black tracks indicate a binary representation of the interaction track of incident proton particles as they move through air and the target material. This neglects the relative intensity of tracks, which would show a greater concentration of tracks tightly packed in the center. The results show a good general agreement with experimentally measured values reported by other investigators using MCNPX [23]. However, unexpected divergence from experimental spectra was noted in the peak intensities for some cases depending on the source of the

cross-section data when using compiled proton table libraries versus physics models built into MCNP6. While the use of proton cross-section libraries is generally recommended when available, these libraries lack data for several less abundant isotopes. This limits the range of their applicability and forces the simulations to rely on physics models for reactions with natural atomic compositions.

3.2.1 MCNP6 Model Limitations

In MCNP6, different cross section libraries are used for the particle-production data corresponding to how the material data cards are coded. When the material is coded as elemental calcium (020000) the particle-production data for protons being used is from 20000.62c library. When the target material is coded as specific calcium isotopes (020AAA) the particle-production data for protons being used is the corresponding 20AAA.80c library. The tabulated neutron and photon creation counts and the PG spectra that result from the two different data libraries are not in agreement. In this case the continuous energy cross-section libraries used as input for our MC simulation are based on evaluated nuclear data files or ENDF/B-VI Release 3 evaluated nuclear data library. This was chosen due to the fact that it is the only one cross section library available containing any tabular data for proton interactions, currently including 48 isotopes.

3.3 MCNP MC Simulation

In the next set of MC simulations the target materials (carbon, calcium oxide, calcium florid, PMMA, and HDPE) are modeled with various mono-energetic incident proton beams (70, 160, 200, 220 MeV). The target material cards are modeled based on the elemental mass fraction as shown in Tab. 2. These MCNP models are used to determine (a) the PG energy spectra from each target and energy combination and (b) the proton range within the target. The PG energy was generated by running a MC simulation software package, MCNP6. The range data was then be compared with the projected proton range determined by CSDA Range, Pstar, and SRIM [31]. The PG yield and the PG relative peak intensities at discrete energies predicted by the MCNP code is compared to similar data previously published and

Table 2: Composition mass percent.

Target	Density (g/cm^3)	H (%)	C (%)	N (%)	O (%)	Ca (%)	F (%)	Ar (%)
PMMA	1.18	8.05	59.99		31.96			
Calcium fluoride	3.18		12			51.3	48.67	
Calcium oxide	3.35				28.53	71.47		
Carbon	2.25		100					
HDPE	0.94	14.37	85.63					
Air, Dry	0.00		0.02	75.51	23.18			1.29

our own experimental results.

In this simulation model the incident proton particles are targeted on a block homogeneous phantom with a depth of 45 cm, which is greater than the projected range of 220 MeV protons in each of the materials. The source is 34.9 cm away from the surface of the target. Both the source and phantom are staged in an environment filled with air. This MCNP6 model tracks the interactions resulting from the mono-energetic proton source that released $1*10^9$ particles at 70, 160, 200 or 220 MeV respectively from a disk source, 1 cm radius, uni-directionally towards the target, in the +z direction. This model neglects any energy straggle or degradation of the incident protons due to generation or interaction with the beam nozzle as they are released and any interactions structural or stabilization equipment (e.g. couch) that would potentially interfere.

MCNP6 simulations for this work used the default Bertini internuclear cascade model, the multi-step pre-equilibrium and evaporation model. The max energy for tracked protons is set to 250 MeV and the Vavilov model for charged particle straggling is used rather than continuous slowing-down approximation. The max energy for tracked neutrons is set to 280 MeV and 10 MeV for photons. Coherent (Thompson) scattering is turned on but the photoneuclear particle production is turned off (alternative is sampling one photon interaction per collision). All neutron and proton nuclear interactions are processed and delayed neutrons are treated as prompt. Doppler broadening was turned on and delayed gammas are not generated.

The range of the incident proton beam is determined by tracking the change in proton
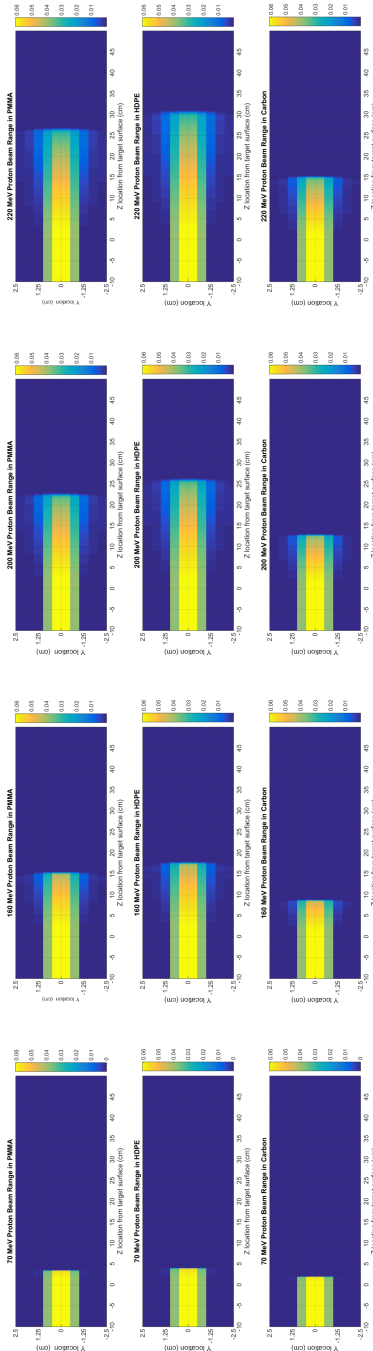
Figure 9: Pulse-height image generated based on the MCNP6 FMESH tally to determined flux of the incident proton providing an indication of particle range. The incident beam energy from top to bottom: 220 MeV, 200 MeV, 160 MeV, 70 MeV. The target material from left to right: PMMA, HPDE, Carbon. The images show that increased energy results in increased depth and that changes slight changes to tissue composition and density influence the range of the incident particles. The fluence reported for each 0.1 mm grid was determined with a relative statistical uncertainty of less than 0.008%

Table 3: Incident proton range (cm), R_{80}: The determined range values indicate the depth at which the initial fluence drops by 50%. Values are reported in centimeters $\pm 0.01 cm$.

Material	Energy	(MeV)		
	70	160	200	220
HPDE	4.01	17.45	25.49	29.60
PMMA	3.49	15.12	22.07	25.59
C	2.00	8.64	12.65	14.83
CaF	1.63	6.95	10.15	11.90
CaO	1.54	6.55	9.59	11.26

fluence along the beam path in 0.1 mm increments along the z-axis, with an FMESH4 tally. These results are graphically expressed in the pulse-height images displayed in Fig. 9. The incident beam energy from top to bottom: 220 MeV, 200 MeV, 160 MeV, 70 MeV. The target material from left to right: PMMA, HPDE, carbon. The range is determined to be the depth at which the proton fluence drops to 50% of its initial fluence, which corresponds to 80% of the max dose point on a depth dose curve, R_{80}. The proton range (R_{80}) results are tabulated in Tab. 3. The results shown in Fig. 9 were found to be in agreement when compared with the expected range and lateral straggling predicted by SRIM 2013 data.

To further validate the range produced by the MC model, the range results are normalized by their density and compared with the data available on Pstar for common elements and compounds, carbon, PMMA, HDPE, and calcium fluoride, the relative statistical uncertainty of the density normalized range (g/cm^2) are all less then 1%. These results are in agreement with the published values within 4%. They were also compared with the CSDA range calculation to provide a reference in the absence of Pstar data. In this case the CSDA range calculation based on the integration of T_{max} to 0.1 MeV and the stopping power was calculated based on composition and additive fractional composition, see Tab. 2. This was done to provide a reference in the absence of Pstar data and to validate the use of additive fractional composition for the use with compounds without established accepted values currently available. The results are again in agreement within 4% and the results are listed in Tab. 4. Having determined the normal behavior of the proton interactions in this model the PG yield are evaluated.

Table 4: Range comparison: The relative statistical uncertainty of the density normalized range determined by MCNP is less than 0.007%. *Calculated values are in agreement within 5%.

Material	T (MeV)	dt/dx Range (g/cm^2) from T$_{max}$ to 0.1 MeV	Pstar CSDA Range (g/cm^2)	MCNP Range (g/cm^2)
Hydrogen	70.00	1.92	1.91	N/A
Hydrogen	160.00	8.36	8.39	N/A
Hydrogen	200.00	12.30	12.38	N/A
Hydrogen	220.00	14.47	14.59	N/A
Carbon	70.00	4.60	4.58	4.51
Carbon	160.00	19.70	19.84	19.52
Carbon	200.00	28.85	29.17	28.58
Carbon	220.00	33.90	34.34	33.50
Oxygen	70.00	4.73	4.69	N/A
Oxygen	160.00	20.21	20.22	N/A
Oxygen	200.00	29.59	29.71	N/A
Oxygen	220.00	34.75	34.91	N/A
Calcium fluoide	70.00	5.15	5.27	5.17
Calcium fluoide	160.00	21.78	22.49	22.09
Calcium fluoide	200.00	31.81	32.96	32.26
Calcium fluoide	220.00	37.33	38.75	37.83
PMMA	70.00	4.03	4.19	4.11
PMMA	160.00	17.27	18.11	17.84
PMMA	200.00	25.30	26.67	26.04
PMMA	220.00	29.73	31.39	30.19
HDPE	70.00	3.7653	3.82	3.76
HDPE	160.00	16.20	16.60	16.40
HDPE	200.00	23.76	24.43	23.96
HDPE	220.00	27.92	28.76	27.82
Calcium oxide	70.00	5.09	N/A	5.14
Calcium oxide	160.00	21.49	N/A	21.93
Calcium oxide	200.00	31.38	N/A	32.11
Calcium oxide	220.00	36.82	N/A	37.70

Table 5: Photon yield: values are reported as photons counted, from 0 to 10 MeV, per source particle. The relative statistical uncertainty of the photon count measurements are all less then 0.04%.

Material	Energy	(MeV)		
	70	160	200	220
C	0.00904	0.0396	0.0595	0.0707
PMMA	0.00972	0.0407	0.0598	0.0698
HPDE	0.00684	0.0300	0.0443	0.0518
CaO	0.0329	0.133	0.196	0.231
CaF$_2$	0.0394	0.150	0.218	0.256

A cylindrical detector surface surrounds the target with a 40 cm diameter. The photon particles were tracked with a surface tally as they crossed this surface in order to determine the absolute yield of secondary prompt gammas produced from the proton interactions. Tab. 5 tabulates the yield of gamma-ray from 0 to 10 MeV to cross the detector surface. The statistical uncertainty of the photon count measurements are less then 0.04%. Fig. 10 compares this gamma-ray yield versus the normalized beam particle range for the materials evaluated. Two distinct slope trends emerge, one for materials composed of oxygen, carbon, and hydrogen and another for those containing calcium. This suggests that the gross gamma-ray yield alone does not provide enough information to independently indicate range verification.

The photon energy data was also collected and the energy distribution was scored in 10 keV bins from 0 to 10 MeV, with a relative statistical uncertainty of less then 1% in all bins with count rates greater than 10^{-6} photons per source particle. The resulting energy spectra are used to compare the discreet peaks of oxygen, carbon and calcium at 6.1 MeV, 4.44 MeV, and 3.74 MeV, respectively, over various energies and chemical compositions. We chose to primarily focus on these discrete energy peaks based on the consensus of previous work indicating that the 6.1 MeV energy peak is a result of the $^{16}O(p, x'\gamma_{6.18})^{16}O$ and $^{16}O(p, p'\gamma_{6.13})^{16}O$ nuclear reactions and that the 4.44 MeV energy peak results from both the $^{16}O(p, x'\gamma)^{12}C$ and the $^{12}C(p, p'\gamma)^{12}C$ reaction. The 3.74 MeV energy peak is the result of the $^{40}Ca(p, p'\gamma)^{40}Ca$ nuclear reaction with a 100% intensity while ^{40}Ca is 96.94%
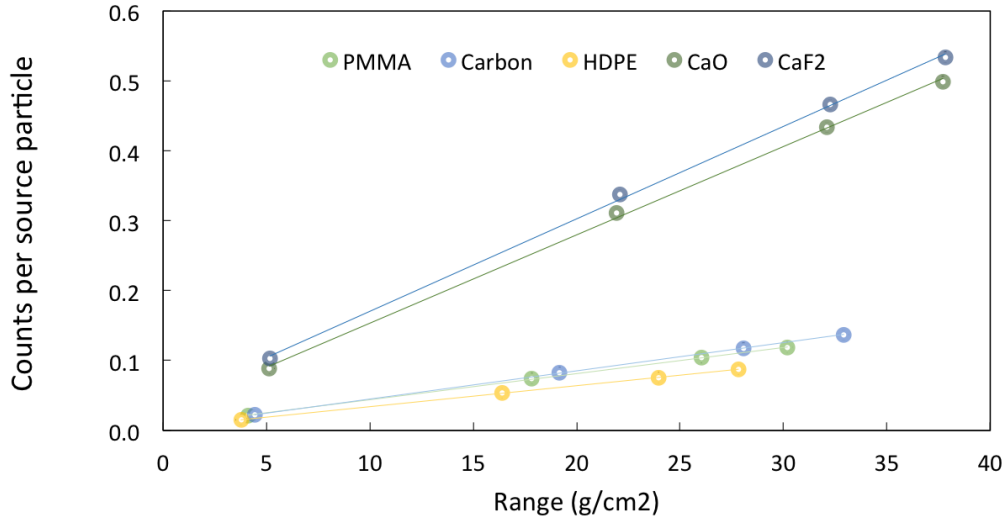
Figure 10: Gross gamma-ray yield, from 0 to 10 MeV, versus the density normalized beam particle range for the materials evaluated. Two distinct slope trends emerge, one for materials composed of oxygen, carbon and hydrogen and another for those containing calcium. This suggests that the gross gamma-ray yield alone does not provide enough information to independently indicate range verification. The uncertainty of the photon count measurements are all less then 0.03% and the range measurement (g/cm^2) uncertainty are less then 1%.

abundant (^{44}Ca accounts for the majority of the remaining abundance and is not reported to produce this discreet energy PG).

Fig. 11 shows the full photon energy spectrum simulated from 0 to 7.5 MeV and light gray lines in the background highlight the energy range of interest. The results from carbon, PMMA, and HDPE are shown in the first graph and calcium oxide, calcium fluoride, and PMMA are shown in the second (the spectra are separated for improved viewing and PMMA is shown on both for relative comparison). The middle and bottom plots of Fig. 11 zoom-in on the regions of interest from 3 MeV to 7 MeV and 5 MeV to 7 MeV respectively showing the calcium 3.74 MeV in calcium oxide and calcium fluoride on the right and its absence in the carbon, PMMA, and HDPE spectrum.

The 3.74 MeV intensity plot, seen in Fig. 12, supports a linear correlation between the 3.74 MeV peak intensity versus mass fraction of calcium by percentage. While J. Polf has reported that the 4.44 MeV intensity correlated to the combined carbon and oxygen composition in homogeneous targets of increasing sucrose concentrations, our results, seen
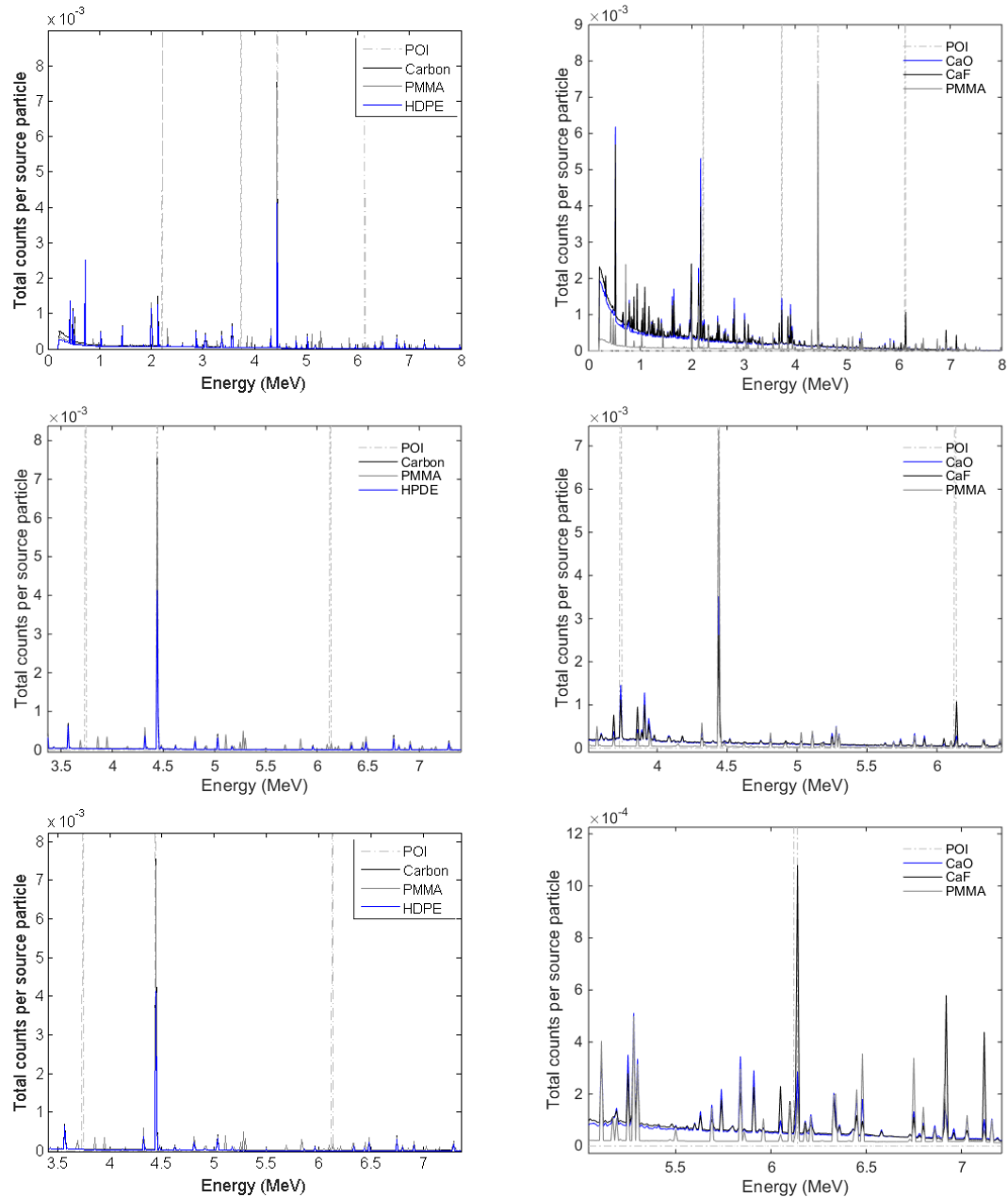
Figure 11: MCNP6 energy spectrum resulting from the total photon yield. The results from carbon, PMMA, and HDPE are shown on the left plot and calcium oxide, calcium fluoride, and PMMA are shown on the right. The light gray lines in the background highlight the energy range of interest at 6.13 MeV, 4.44 MeV, and 3.74 MeV. The photons are tallied in 10 keV bins with a statically relative uncertainty of less than 1% for all bins with count rates greater than 10^{-6}. Top: MCNP6 energy spectrum resulting from the total photon yield from roughly 0 to 8 MeV. Middle: MCNP6 energy spectrum resulting from the total yield of gamma-ray from roughly 3 to 7 MeV showing the calcium 3.74 MeV in calcium oxide and calcium fluoride on the right and its absence in the carbon, PMMA, and HDPE spectrum. Bottom: Energy spectrum resulting from the total yield of gamma-ray from roughly 3 to 7 MeV.
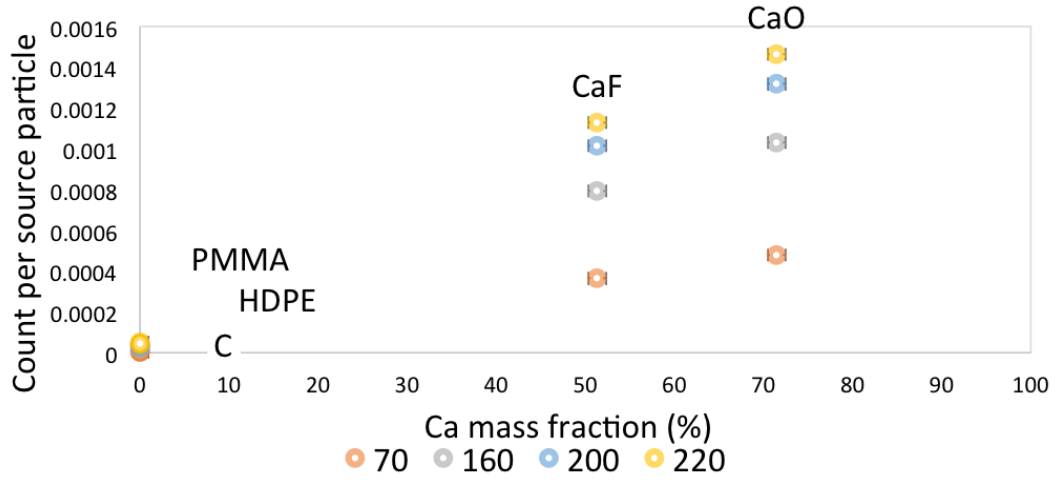
Figure 12: Peak intensity (counts per source particle) versus mass fraction of target material. This plot suggests a linear correlation between the 3.74 MeV peak intensity versus the calcium mass fraction of each target.

in Fig. 13, are not as clear. [24] The results from the carbon, PMMA, and calcium oxide trend toward a near linear correlation, however, the HDPE target data does not follow this trend. Further, Fig. 13 shows a divergence of the peak intensity over the investigated incident energy range. The three plots of Fig. 14 shows that our 6.13 MeV results do indicate a peak that corresponds with the presence of oxygen, however the results do not correspond well with the mass fraction of oxygen in our targets. They suggest that calcium and fluorine may contribute to the total intensity calculated for this peak. However, since fluorine accounts for less than 1% of human composition it may not significantly interfere with interpretation for clinical applications and thus it may be appropriate to ignore this contribution. Fluorine is reported to result in a PG of 6.13 MeV with an intensity of 56% from the following nuclear reactions according to the National Nuclear Data Center (NNDC), $^{19}F(p,p')^{19}F$ and $^{19}F(p,x)^{19}F$. However NNDA does not report any ^{40}Ca or ^{44}Ca reaction resulting in a discreet 6.13 MeV peak.
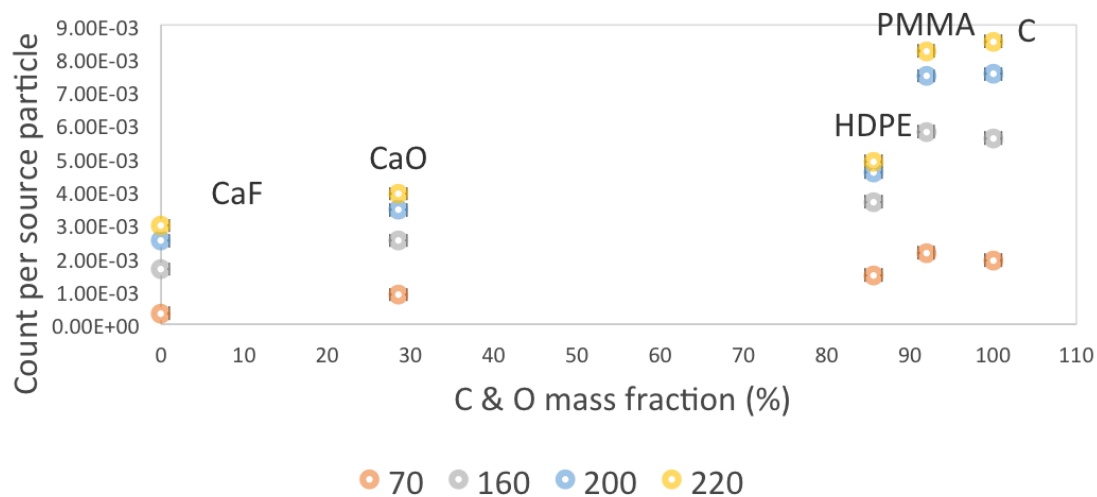
Figure 13: Peak intensity (counts per source particle) versus mass fraction of target material. This plot shows the intensity of the 4.44 MeV peak versus the combined carbon and oxygen mass fraction of each target. This shows a general agreement for the carbon, PMMA, and the CaO target data but the HDPE does not fall in with a linear trend trend. Note, this combined mass fraction summation does not account for the 4.44 MeV peak intensity seen in the CaF_2 is a result of interactions with fluorine. It may be appropriate to ignore this 'contamination' as fluorine accounts for less than 1% of the composition of the human body, thus would not significantly interfere with interpretation for clinical applications.
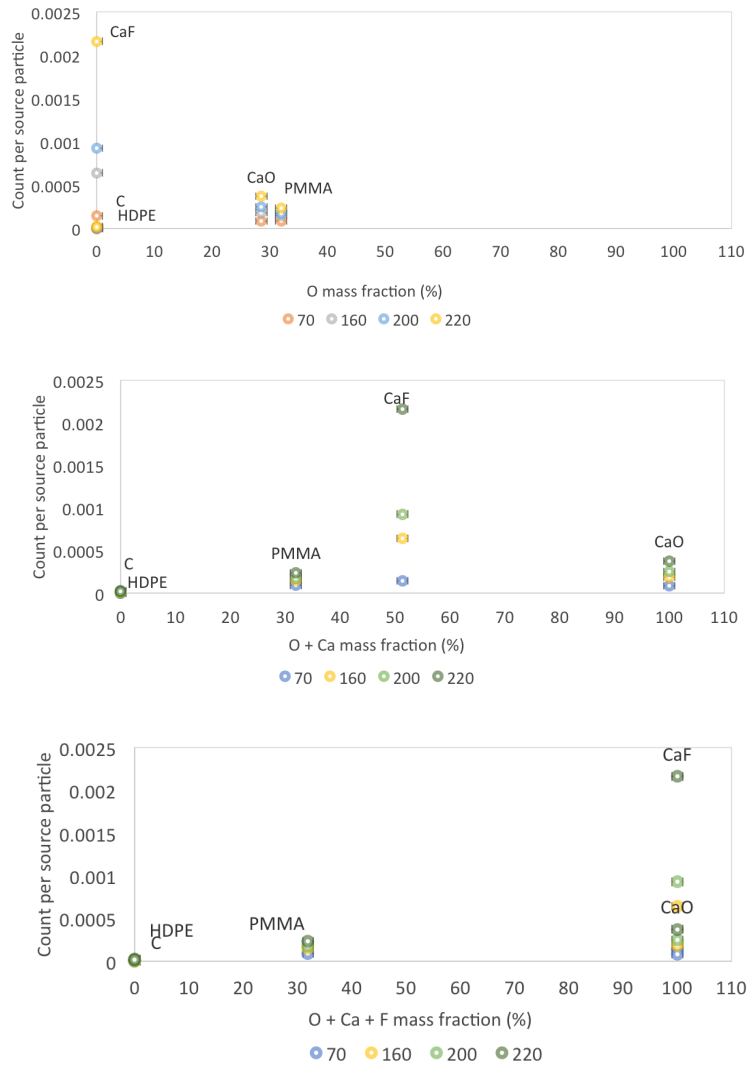
Figure 14: Peak intensity (counts per source particle) versus mass fraction of target material. The first plot shows the intensity of the 6.13 MeV peak versus the mass fraction of oxygen in each target. The mass fraction of oxygen alone does not account for the relative 6.13 MeV peak intensities. The second plot shows the intensity of the 6.13 MeV peak versus the combined oxygen and calcium mass fractions of each target. The third plot shows the intensity of the 6.13 MeV peak versus the oxygen, calcium, and fluorine mass fraction of each target. Of the targets evaluated in this study the best agreement is seen in the third plot the oxygen, calcium, and fluorine mass fraction of each target however since fluorine accounts for less than 1% of human composition it may not significantly interfere with interpretation for clinical applications and thus it may be appropriate to ignore this contribution.

CHAPTER IV

EXPERIMENTAL VERIFICATION

The MC simulations are contingent on the availability and accuracy of the proton cross-section data used which is limited in scope of material and incident energy thus limiting the authenticity of the output energy spectrum produced. When the cross-section data of interest is not available from tables, the simulation defaults to interpolation or general physics models, thus producing different results. This divergence was seen in our preliminary work when the material cards were coded with natural elements versus specific element isotopes in naturally occurring ratios. In addition, previous publications and our preliminary simulations indicated a tendency of MC simulations to under estimate the effects of Doppler broadening in peaks of interest, particularly for carbon around the 4 MeV range. The following experimental work was done to address these concerns and provide some means of benchmarking to increase confidence in the MCNP MC results produced. Further these results support the expectation that detection of PG in clinical environments at treatment levels is possible.

4.1 Benchmark Experimental Design

In order to benchmark our MCNP simulation results, a series of experiments measuring the PGs emitted from various targets composed of carbon, oxygen, and hydrogen were performed. The resulting PG energy spectra ratios are then compared to those produced by the MCNP simulations.

Northwestern Medicine Chicago Proton Center (CPC) is located 30 miles west of Chicago. It houses an IBA 51230 cyclotron that supplies their proton beams. With this state-of-the-art equipment they are able to offer treatment plans covering an energy range of roughly 70-220 MeV at snout of the beam nozzle. CPC also employs pencil beam scanning technology that allows precise beam targeting [6].
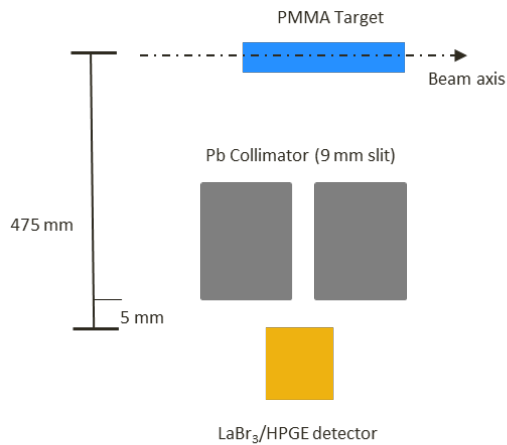
Figure 15: Left: Schematic illustration of experimental setup, not to scale. Right: Experimental set-up at CPC. An IBA ST-230 cyclotron was used to generate a mono-energetic proton beam at 220 MeV. A universal nozzle focuses and directs the incident pencil spot beam onto the center of the identified target materials. The cerium-doped lanthanum(III) bromide ($LaBr_3$:Ce) detector and a HPGE were placed 475 mm from the center of the target phantom at ninety degrees with respect to the incident beam axis. A lead brick collimator with a 9 mm slit was placed 5 mm distal to detector surface to allow for location specific assessment.

Experimental measurements were taken at CPC in order to evaluate MC simulations produced by MCNP6. As shown in Fig. 15, an IBA ST-230 cyclotron was used to generate a mono-energetic proton beam at 220 MeV. A universal nozzle focuses and directs the incident pencil spot beam onto the center of the identified target materials (carbon, PMMA, and HDPE). In order to measure the resulting PGs emitted, a cerium-doped lanthanum(III) bromide ($LaBr_3$:Ce) detector and a high purity geranium (HPGE) detector were placed 475 mm from the center of the target phantom at ninety degrees with respect to the incident beam axis. A lead collimator with a 9 mm slit was placed 5 mm distal to detector surface to allow for location specific assessment. Fig. 15 shows the experimental room set-up. The 220 MeV beam energy was run with a current of 180 nA. Each measurement was collected for approximately 3840 MU over 5 minutes.

4.1.0.1 Targets

In turn each target was positioned at the center of the couch within the beam-line and the target depth of interest was aligned at beam iso-center for each measurement. Data collection was initiated at the depth just beyond the anticipated Bragg peak deposition for each target material. The couch was translated in 10 mm increments along the beamline in order to shift the desired target depth to the measurement point. The 2.5 x 2.5 x 40 cm^3 PMMA blocks were provided. The HDPE sample, from Argonne National Laboratory in Chicago, is 2.5 inches in diameter and 21 inches long. 4 x 4 x 20 in^3 graphite blocks composed of carbon was sourced from Georgia Institute of Technology.

4.1.0.2 Detectors

LaBr3:Ce (LaBr) detector was used to measure the emitted photon spectra. The detector is a medium-resolution scintillation detector comprised of a 1.5 cm x 1.5 cm LaBr crystal and a photomultiplier tube (PMT) with an internal magnetic shield manufactured by Canberra. This detector was chosen for its high energy resolution compared to other scintillators, and improved linearity and efficiency with short decay times (16 ns) relative to NaI(TI) crystals [25, 5].

A second HPGE detector was also used to collect the emitted photon spectra. This detector is a high-resolution semi-conductor diode manufactured by Canberra. These detectors are well accepted for their excellent energy resolution, particularly for photons, allowing for the resolution of tightly packed peaks that remain unresolved in most scintillation detectors currently available.

4.1.1 Energy Calibration

The facility did not have any calibration check sources available in the anticipated region of interest between 2-10 MeV. As a result, the energy calibration is based on check source measurements performed with the same equipment and settings at Georgia Institute of Technology. The points used include Co-60 (1332.5 keV, 1173.2 keV), Cs-137 (662 keV),

PuBe (4438.9 keV, 3927.9 keV, 3416.9 keV), and Th (583.1 keV (Ti-208), 911.1 keV (Ac-228), 969.1 keV (Ac-228), and 2614 keV (Ti-208)), as well as the internal decay signature of the LaBr$_3$:Ce detector at 1436 keV. The calibration curves were then confirmed through verification of the internal LaBr decay signature and naturally occurring thorium decay products in the background experimental measurements as well as the annihilation peak at 0.511 MeV in beam-on experimental measurements.

4.1.2 Background Radiation

The background spectrum was evaluated to verify that remaining background or activation from earlier clinical treatments were not at a statistically significant level that would interfere with the data collection. Due to limited room-time and beam-time, individual background measurements were not taken between each run, however, a ten minute background of the target was taken at the end of the beam-time to quantify the activation of the target as well as a ten minute background with the target removed from the beam line.

4.1.3 Experimental Data

LaBr$_3$:Ce data was acquired for the carbon, PMMA, and HDPE targets. Unfortunately, these data did not provide any useful insight or method validation due to the limited energy resolution and constrained energy calibration. The HPGE detector was used to collect data for the PMMA target and, as would be expected, provided improved energy resolution allowing for the identification and quantification of several regions of interest. Fig. 16 shows the full cumulative spectra collected on a log-scale. The 6.1 MeV peak and its single and double escape peak, at 5.6 MeV and 5.1 MeV can already be identified.

After the post-beam-time background was subtracted to remove activation background from the spectrum a ROOT subtraction was applied. This was done in order to further improve the resolution by removing some of the continuous energy data. Fig. 17 shows a section of the spectrum with various iteration levels that could be removed via this subtraction method. Ten iterations were used for the following plots as it was the best fit for the energy range of interest for 2 MeV to 8 MeV.

Fig. 18 shows the PMMA cumulative energy spectra from 4.5 MeV to 7.5 MeV collected
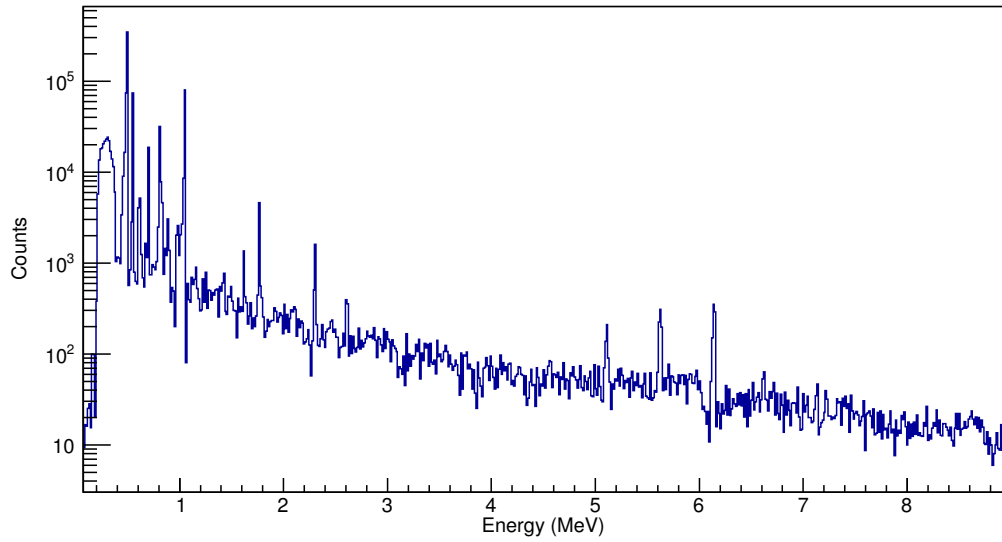
Figure 16: PMMA cumulative energy spectra from 0 MeV to 9 MeV collected with an HPGE detector.
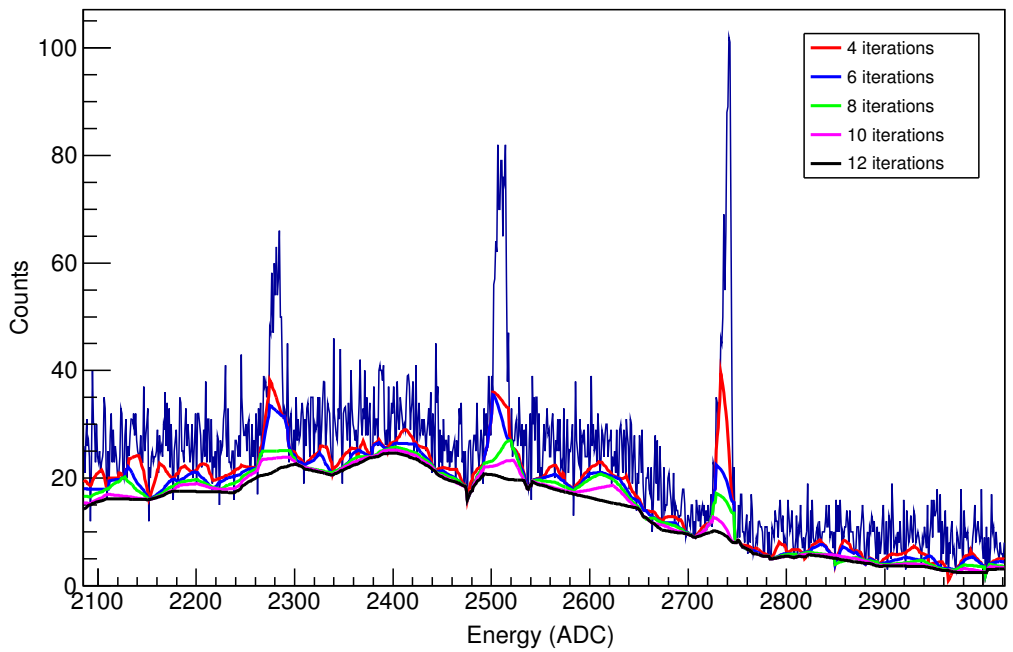
Figure 17: ROOT subtraction method applied to improve resolution. The 10 iterations line was selected as the best fit for the energy range of interest.
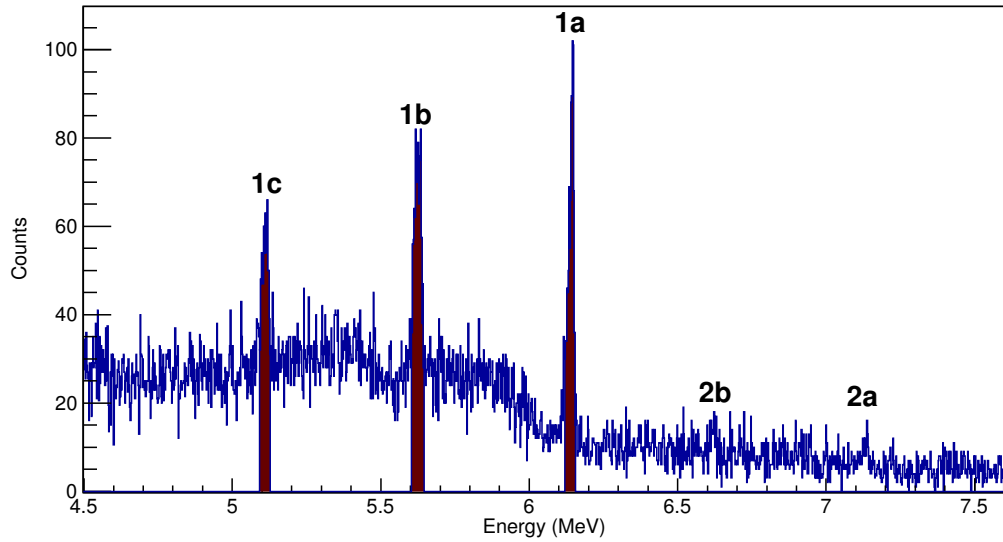
Figure 18: PMMA cumulative energy spectra from 4.5 MeV to 7.5 MeV collected with an HPGE detector. (1a) 6.1 MeV peak, (1b) single escape peak 5.6 Mev and (1c) double escape peak 5.1 MeV. The 7.1 Mev from oxygen and its single escape peak is also labeled, (2a) and (2b) respectively.

with an HPGE detector. The 6.13 MeV integrated area is highlighted in red and the full energy peak integral is equal to 928 counts over 16 bins. The single and double escape peak integrals result in 1163 counts and 804 counts respectively over 16 bins each. The 7.1 Mev from oxygen and its single escape peak is also labeled, (2a) and (2b) respectively. Fig. 19 highlights the 4.44 MeV and 6.13 MeV peaks and their corresponding double and single escape peaks after the data was re-binned. The 4.44 MeV integrated area is high-lighted in green. The full energy peak integral is equal to 268 counts over 6 bins. The single and double escape peak integrals result in 393 counts over bin 6 bins and 363 counts over 4 bins respectively.

4.1.4   Data Evaluation

The results generated by the MCNP models are idealized data sets resulting in sharp clean peaks relative to the obtainable experimental results. There are a number of factors that contribute to this effect. The MC models are able to track each particle history, counting every flagged photon that crosses the identified surface of interest representing the detector,
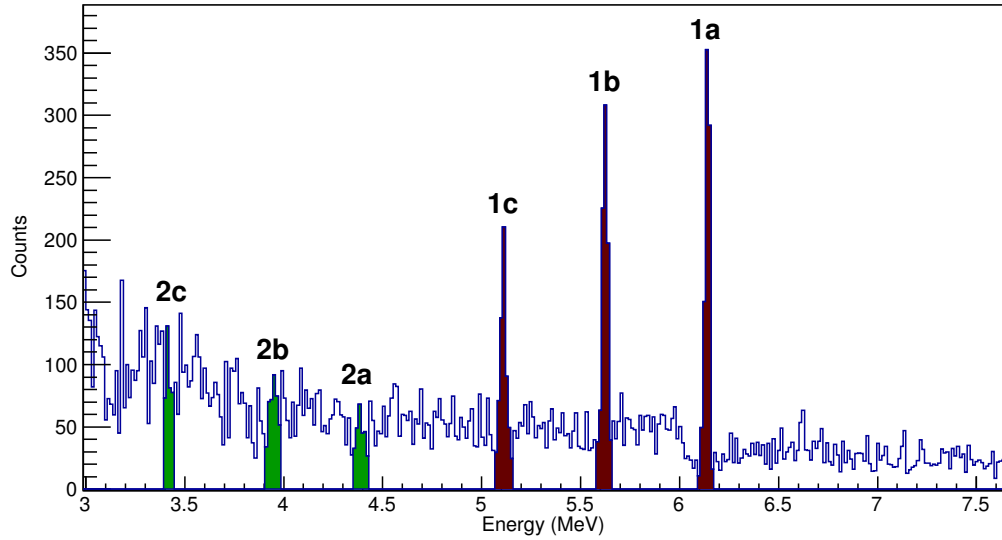
Figure 19: HPGE PMMA cumulative Energy spectra from 3.5 MeV to 7.5 MeV ROOT re-binned for improved resolution around the 4 MeV range. The (2a) 4.44 MeV peak, (2b) single escape peak 3.9 MeV and (2c) double escape peak 3.4 MeV labeled and integrated area is highlighted in green. The (1a) 6.1 MeV peak, (1b) single escape peak 5.6 Mev and (1c) double escape peak 5.1 MeV labeled and integrated area is highlighted in red.

thus providing the equivalent of 100% detection efficiency. Unfortunately, this efficiency rate is not possible in application. Experimental data are limited by the detector's ability to "convert the kinetic energy of charged particles in light" and "the light into an electrical pulse" [11] as well as the decay time of the induced luminescence of the scintillation crystal.

Further, the MC model is counting photon flux, which is essentially equivalent to assuming 100% energy deposition, thus we see less Compton scatter in our simulation spectra as well as an absence of single and double escape peaks. In reality this is one of the primary challenges faced by detectors, particularly at this energy range. Here they are attempting to balance the need for a thick enough detector to allow full energy deposition while still being thin enough to allow the signal to reach the PMT.

The particle flux rate experienced in a clinical setting is very fast, on the order of $5 * 10^9/cm^2/s$. This creates challenges for current detectors. The high flux rate results in new signals activating the scintillation crystal before the induced luminescence from the previous signal has had adequate time to decay. This is known as pulse pile-up and results

in detector dead-time due to its inability to process additional signals until the induced luminescence drops below its threshold. This efficiency limitation effectively limits the available counting statistics within each run at such high flux rates. This is particularly true of detectors with a high energy resolution. This does not hinder the MCNP MC models as they do not take time into consideration and flux rates are effectively simplified to fluence for the purpose of simulations.
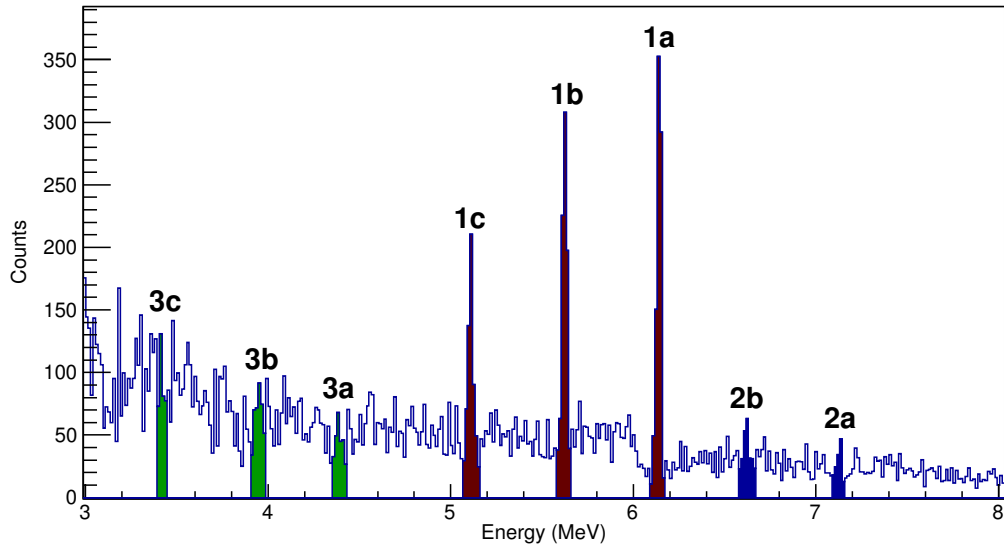
Figure 20: HPGE PMMA cumulative Energy spectra from 3 MeV to 7 MeV ROOT re-binned for improved resolution around the 4 MeV range. The full energy deposition peak, (1a), and the single, (1b), and double, (1c), escape peaks for the 6.13 MeV peak are highlighted in red; the full energy deposition peak, (2a), and the single, (2b), and double, (2c), escape peaks for the 4.44 MeV peak are highlighted in green; the full energy deposition peak, (2a), and the single escape peak, (2b), for the 7.12 MeV peak are highlighted in blue. The double escape peak is not distinctly visible as it is buried within the full energy deposition peak of 6.13 MeV.

4.2   Verification with MNCP6 Model

In an effort to show agreement between the results generated from MCNP6 and our experimental evaluation the peak intensity ratios for the 6.13 MeV and 7.12 MeV are compared. The full energy deposition peak, (1a), and the single, (1b), and double, (1c), escape peaks for the 6.13 MeV peak are highlighted in red the full energy deposition peak, (2a), and the

Table 6: Integration of peaks highlighted in Fig. 20. * Indicates calculated counts.

Energy$_\gamma$ (MeV)	Peak label	Peak integral (counts)
4.44	3a	268 ± 16
	3b	393 ± 20
	3c	363 ± 19
6.13	1a	728 ± 48*
	1b	1163 ± 34
	1c	804 ± 28
7.12	2a	170 ± 13
	2b	333 ± 18
	(2c)	200 ± 18*

single escape peak, (2b), for the 7.12 MeV peak are highlighted in blue in Fig. 20. The 7.12 MeV double escape peak is not distinctly visible as it is buried within the full energy deposition peak of 6.13 MeV. As a result, the area under the peaks could not be simply integrated, summed and compared. Instead the single escape peak for each energy was integrated and normalized by the germanium pair production in nuclear field cross section. The resulting intensity ratio of the 7.12 Mev to 6.13 MeV peak intensity, 0.248 ± 0.02, was found to be in good agreement with that produced by our simulation, 0.262 ± 0.002. This result is in agreement within 5.4%. These results are shown in Tab. 7. Making the assumption that the single escape and double escape ratio is the same, the 7.12 MeV double escape peak could be calculated and separated from the full energy deposition of the 6.13 MeV peak. The resulting measured counts are listed in Tab. 6. This allowed for the summation of the count contribution from each energy, which was then normalized by the germanium total cross section. The resulting intensity ratio of the 7.12 Mev to 6.13 MeV peak intensity, 0.261 ± 0.03, was found to be in good agreement with that produced by our simulation, 0.262 ± 0.002 as shown in Tab. 8. This result is in agreement within 0.2%

Table 7: Evaluation of 6.13 MeV and 7.12 MeV double escape peak ratio from experimental data and MCNP6 simulation. This result is in agreement within 5.4%.

Photon Energy (MeV)	S.E. Integral (counts)	Ge P.P. nuc cross-section (cm^2/g)	Integral Norm	MC Intensity (photons/s.p)	Peak 1:2 ratio experimental	Peak 1:2 ratio MCNP
4.44	394	0.008027	49046	0.00822		
6.13	1162	0.01164	99871	0.000235		
7.12	333	0.01341	24847	0.0000615	0.24 ± 0.02	0.26 ± 0.002

Table 8: Evaluation of 6.13 MeV and 7.12 MeV detection ratio from experimental data (summing counts from full energy deposition, and single and double escape peaks) and MCNP6 simulation. This result is in agreement within 0.2%.

Photon Energy (MeV)	Sum Integral (counts)	Ge total cross-section (cm^2/g)	Integral Norm	MC Intensity (photons/s.p)	Peak 1:2 ratio experimental	Peak 1:2 ratio MCNP
4.44	1024	0.03217	31839	0.00822		
6.13	2694	0.03104	86822	0.000235		
7.12	703	0.03095	22727	0.0000615	0.26 ± 0.03	0.26 ± 0.002

CHAPTER V

DISCUSSION OF SOURCES OF UNCERTAINTY

5.1 Source of Uncertainty in Proton Therapy

The application of the distinct therapeutic advantages of proton therapy are currently limited due to the relatively large overall uncertainty in dose delivery. A number of contributing factors including, but not limited to, uncertainty due to imaging, patient setup and motion, beam delivery, dose calculation and approximations, material constants, CT conversions, and biological effects [19]. The current method of managing these uncertainties is to incorporate larger treatment margins to ensure tumor coverage. Current standard practice is an increased treatment margin of 2.5%+1.5mm to 3.5%+3mm [19], which is designed to compensate for 1% patient set-up, up to 2% for I-values and $\sim 4\%$ for tissue densities.

5.1.0.1 Range Measurement

Ideally particle range would be defined at 80% of max dose. This is the point at which 50% of protons have stopped for a mono-energetic beam and this point is relatively independent of the beams energy distribution. However, for historical reasons, since photons and electron range is measured at 90% maximum dose, proton range is clinically measured at 90% of maximum dose [20].

5.1.0.2 Tissue Composition

Particle range is dependent on the electron density and the atomic fraction of the medium(s) the particle travels through. This calculation is relatively straight forward when the particle is traveling through homogeneous material; however, this becomes more complicated to compute as the particle travels through multiple layers of heterogeneous materials and similar materials composed of varying tissue compositions. The human body is made up of several different tissue types and organ size is patient specific. Thus size and composition should be determined on an individual basis for the region of interest. Slight variations

in tissue composition can also occur, especially for oxygen concentration between healthy and unhealthy tissue regions. Since patient specific organ size and exact tissue composition is difficult to determine directly, this information is currently determined indirectly through some form of imaging. As a result, these indirect measurements and conversions add additional uncertainty to the range calculation.

5.1.0.3 *Mean Ionization Energy*

Another important variable in determining stopping power, based on Bethe-Bloch formula, is the mean excitation energy, which is an empirically determined value. Previous research by Andreo et al. [1] has shown that there are significant uncertainties in the mean excitation energy, I-value, due to tissue composition and particle energies thus 'ICRU-44 recommends that body tissue not be treated as a physical constant.' "It was concluded that the range uncertainty due to uncertainties in I-values is on the order of $\pm 1.5 - 2.0\%$. The difference in I-value between 75 and 80 eV results in a $0.8 - 1.2\%$ difference in the predicted stopping power in the therapeutic energy range." [1]

5.2   Uncertainty in Monte Carlo calculations

There are several components that contribute to the uncertainty associated with the MC results produced by the MCNP code including statistical sampling, interaction cross-sections, geometry, and source signal.

5.2.1   Statistical

The code provides an internal evaluation of ten statistical tests to provide users with an indication of how well (precise) the tally converges on the final answer. This does not provide the user with any indication of the accuracy of the result but rather that all of the histories sampled converge toward a consistent result. If a simulation fails to pass any of the tests, adjustments should be made to rectify the discrepancy, such as increasing the number of histories run.

5.2.2 Cross-section

The particle cross-sections indicate the probability of particle interaction. The code obtains this information from large tabulated data sets, known as libraries, for various particle types, energies, materials (for limited elements and isotopes), and limited temperature and density options. Only one library containing proton cross-sections is currently available for MCNP6, which includes information for a total of 48 elements. The cross-section uncertainty values (probability distribution) for this published data set is not currently available.

5.2.3 Geometry

The geometry of the environment, including the physical dimensions of cells, material densities, and material composition also contribute to the uncertainty of the calculated results. This could be evaluated with the PERT card which randomly varies the input and produces two outputs (with and without the variation). In this simulation this was not performed as it was assumed to be accurate within detectable limits.

5.2.4 Calculation of source and detector signal

There are also uncertainties associated with changes in starting energies of source particles. This takes place due to degradation of the incident energy and divergence resulting from interactions with the nozzle or other components of the accelerator. This is often difficult to simulate due to lack of or limited knowledge of exact 'nozzle' design due to limits on the the information provided by manufacturers. This could be investigated with the use of the ISO spectra modifier, however, this was ignored in this simulation as it was performed with a mono-energetic beam.

5.3 Quantification of Experimental Uncertainty

5.3.1 Systematic physics uncertainties

Systematic physics uncertainties includes consistent or fundamental errors introduced to an experimental system based on equipment or experimental design. This is when the same error consistently influences every measurement the same way resulting in all of the data

collected being recorded over or under the true measurement in a consistent direction. Multiple data collection equipment or measurement methods may needed in order to determine if this type of error is introduced into the system since the error is fundamental in the setup.

Steps that may have introduced systematic physics uncertainties into the experimental system discussed here include but are not limited to: normalization with respect to the number of ions, MU measurement system of the treatment system, background subtraction procedure, and the geometrical description of each setup including the detector field of view and the solid angle.

5.3.2 Statistical physics uncertainties

Statistical physics uncertainties are random error within the system. As with computational measurements it is important to collect enough data points with a large enough signal to provide a normalized distribution around the true value. This component of uncertainty is calculated by propagating the variance of each of the individual system components through a function relating these components to the measured results of the system and reporting the square root of the propagated value. This is most often reported as the standard deviation.

CHAPTER VI

CONCLUSION AND RECOMMENDATIONS

6.1 Conclusion

The gross yield of secondary PG from a proton beam at clinically relevant energies of 70, 160, 200, and 220 MeV would not provide a direct indication of an unknown target's RSP. However, the data gravitates towards two distinct slope trends, one for materials composed of carbon and hydrogen and another for those containing calcium. This is likely due to larger proton absorption cross section of calcium. This indicates that this information may be more useful in conjunction with other potentially known variables about the target composition to provide range verification.

The 3.74 MeV energy peak that results from the $^{40}Ca(p,p'\gamma)^{40}Ca$ nuclear reaction shows a linear correlation with calcium composition of the targets. Based on the materials evaluated, the 4.44 MeV peak from $^{16}O(p,x'\gamma)^{12}C$ and $^{12}C(p,p'\gamma)^{12}C$ and the 6.13 MeV peak expected from $^{16}O(p,p'\gamma)^{16}O$ nuclear reactions do not appear unique to the carbon and oxygen inelastic decay. These peaks may still be useful if further studied show that other primary materials in the human body do not contribute significantly to these discrete energies. Otherwise these peaks may require a more sophisticated algorithm that could incorporate composition information from unique peaks to resolve the relative contribution from peaks that result from the summation of multiple reactions.

The experimental work performed to further validate the MC model showed a good agreement between the relative peak ratio determined from experimental data with model prediction. The peak intensity of the 6.13 MeV and 7.12 MeV peaks from oxygen were compared as they were both distinctly identifiable in both data sets and both result from PGs emitted from proton interactions with oxygen. The results indicated that the single escape peak ratio is within 5.4% and the combined peak ratio is within 0.2% of our MC predicted results.

6.2 Future recommendations

6.2.1 Experimental

Experimental studies are very important for future work to provide a means of validation and bench-marking as it is still rather early in the development of this subject matter. Further evaluation of absolute PG yield and gross energy spectra produced from targets composed of the primary elements found in the human body is needed. Of particular interest would be data from materials containing calcium. Additional spectrum from a broader variation of oxygen and carbon material compositions would continue to be beneficial but it is important to be cognizant that the primary peaks being investigated for these materials may not be unique enough to provide a complete picture.

6.2.2 Computational

While it is important to continue experimental work to provide validation and bench-marking of the production of secondary PG and to improve the cross-section data available, it is still useful to pursue computational evaluations to explore and optimize these techniques for range verification. This is especially true due to the limitation in time, cost, and access to proton beam-time. Evaluation of targets containing various concentrations of calcium as well as concentrations of elements commonly found in the human body other than carbon, oxygen, and hydrogen should be investigated to validate that the discrete energy peaks of interest, such as 3.74 MeV for calcium, are unique to the element of interest. It would be useful to determine an algorithm to resolve contributions from the continuum resulting from heavier elements, such as calcium, from oxygen contributions to the 6.13 MeV and 7.12 MeV peaks or identify an alternate unique peak corresponding to oxygen. In conjunction, improved correlation between PG intensity and elemental composition may be resolved by comparing cross-section and threshold energy of the peaks of interest for their impact on count intensity for peaks resulting from multiple contributions. In addition it would be valuable to perform sensitivity analysis due to its dependency on available cross-section data/physics models to evaluate the confidence of this work. As a next step, heterogeneous targets could be evaluated to determine if these correlations hold and that

it is still possible to resolve the characteristic peaks of interest.

Finally, further MC simulated energy spectra should be measured at location specific depths parallel to the beam path and compared with corresponding experimental data. The location specific gross PG yield could provide range verification and the energy spectrum could provide additional insight regarding heterogeneous variations in the target along the beam path.

APPENDIX A

LETTERS OF PERMISSION

Dear Jessica Saunders,

Thank you for your request to reproduce IOP Publishing material in your thesis.

Regarding:

Figure 1 (Phys. Med. Biol. 58 (2013) R131R160)

We are happy to grant permission for the use you request on the terms set out below.

Conditions

Non-exclusive, non-transferrable, revocable, worldwide, permission to use the material in print and electronic form will be granted subject to the following conditions:

- Permission will be cancelled without notice if you fail to fulfil any of the conditions of this letter.

- You will make reasonable efforts to contact the author(s) to seek consent for your intended use. Contacting one author acting expressly as authorised agent for their co-authors is acceptable.

- You will reproduce the following prominently alongside the material:

  o the source of the material, including author, article title, title of journal, volume number, issue number (if relevant), page range (or first page if this is the only information available) and date of first publication. This information can be contained in a footnote or reference note; or

  o a link back to the article (via DOI); and

  o if practical and IN ALL CASES for works published under any of the Creative Commons licences the words " Institute of Physics and Engineering in Medicine. Reproduced by permission of IOP Publishing. All rights reserved."

- The material will not, without the express permission of the author(s), be used in any way which, in the opinion of IOP Publishing, could distort or alter the author(s)' original intention(s) and meaning, be prejudicial to the honour or reputation of the author(s) and/or imply endorsement by the author(s) and/or IOP Publishing.

- Payment of £0 is received in full by IOP Publishing prior to use.

If you have any questions, please feel free to contact our Permissions team at permissions@iop.org.

I should be grateful if you would acknowledge receipt of this email.

Kind regards,

Kathryn Shaw

Copyright & Permissions Team

Gemma Alaway Rights & Permissions Adviser

Kathryn Shaw - Editorial Assistant

Contact Details

E-mail: permissions@iop.org

For further information: http://iopscience.iop.org/page/copyright Please note: We do not provide signed permission forms as a separate attachment. Please print this email and provide it to your institution as proof of permission.

REFERENCES

[1] ANDREO, P., "On the clinical spatial resolution achievable with protons and heavier charged particle radiotherapy beams," *Physics in Medicine and Biology*, vol. 54, no. 11, p. N205, 2009.

[2] ATTIX, F., *Introduction to Radiological Physics and Radiation Dosimetry*. Wiley, 1986.

[3] BIEGUN, A. K., SERAVALLI, E., LOPES, P. C., RINALDI, I., PINTO, M., OXLEY, D. C., DENDOOVEN, P., VERHAEGEN, F., PARODI, K., CRESPO, P., and SCHAART, D. R., "Time-of-flight neutron rejection to improve prompt gamma imaging for proton range verification: a simulation study," *Physics in Medicine and Biology*, vol. 57, no. 20, p. 6429, 2012.

[4] BOM, V., JOULAEIZADEH, L., and BEEKMAN, F., "Real-time prompt gamma monitoring in spot-scanning proton therapy using imaging through a knife-edge-shaped slit," *Physics in Medicine and Biology*, vol. 57, no. 2, p. 297, 2012.

[5] Canberra Industries, *Canberra LABR-1.5x1.5LaBr₃(Ce) Scintillation Detector*, 2011.

[6] "Chicago proton center: Explore the center," cited 2015;.

[7] COUTRAKON, G.and BASHKIROV, V., HURLEY, F., JOHNSON, R., RYKALIN, V., SADROZINSKI, H., and SCHULTE, R., "Design and construction of the 1st proton ct scanner," in *Application of Accelerators in Research and Industry*, API Publishing, LLC, 2013.

[8] HPAUL, "Depth dose of electrons, x rays or protons entering human tissue for the purpose of cancer treatment," 2009.

[9] JABBERWOK, "A diagram of a photon hitting a target and bouncing off." English Wikipedia. Transferred from en.wikipedia to Commons., December 2006.

[10] KABUKI, S., E. A., "Study on the use of electron-tracking compton gamma-ray camera to monitor the therapeutic proton dose distribution in real time," *Nuclear Science Symposium Conference Record*, 2009.

[11] KNOLL, G. F., *Radiation Detection and Measurement*. John Wiley & Sons, 2010.

[12] KNOPF, A. and LOMAX, A., "In vivo proton range verification: a review," *Phys Med Biol*, vol. 58, no. 15, pp. R131–60, 2013.

[13] KORMOLL, T., E. A., "A compton imager for in-vivo dosimetry of proton beams: A design study," *Nuclear Instruments and Methods in Physics Research Section A: Accelerators, Spectrometers, Detectors and Associated Equipment*, vol. 626-627, pp. 114–119, 2011.

[14] LANEY, T. D. and KOOY, H., *Proton and Charged Particle Radiotherapy*. Wolters Kluwer Health/Lippincott Williams & Wilkins, 2008.

[15] MARKFILIPAK, "Comparison of dose profiles for proton v. x-ray radiotherapy.png," tech. rep., Wikimedia Commons, $https : //commons.wikimedia.org/wiki/File : Comparison_of_dose_profiles_for_proton_v \cdot x - ray_radiotherapy.png$, October 2012. This was adapted from Figure 1 of "Proton beam therapy" by W P Levin, H Kooy, J S Loeffler, and T F DeLaney, British Journal of Cancer (2005) 93, 849854 downloaded by author from http://www.nature.com/bjc/journal/v93/n8/abs/6602754a.html.

[16] "Monte carlo nparticle transport code system including mcnp6.1, mcnp5-1.60, mcnpx-2.7.0 and data libraries," tech. rep., RSICC, cited Aug 2015.

[17] MIN, C.-H., KIM, C. H., YOUN, M.-Y., and KIM, J.-W., "Prompt gamma measurements for locating the dose falloff region in the proton therapy," *Applied Physics Letters*, vol. 89, no. 18, 2006.

[18] MIN, C.-H., LEE, H. R., KIM, C. H., and LEE, S. B., "Development of array-type prompt gamma measurement system for in vivo range verification in proton therapy," *Medical Physics*, vol. 39, no. 4, pp. 2100–2107, 2012.

[19] MOTEABBED, M., ESPAA, S., and PAGANETTI, H., "Monte carlo patient study on the comparison of prompt gamma and pet imaging for range verification in proton therapy," *Physics in Medicine and Biology*, vol. 56, no. 4, p. 1063, 2011.

[20] PAGANETTI, H., "Range uncertainties in proton therapy and the role of monte carlo simulations," *Phys Med Biol*, vol. 57, no. 11, pp. R99–117, 2012.

[21] PARK, M.-S., LEE, W., and KIM, J.-M., "Estimation of proton distribution by means of three-dimensional reconstruction of prompt gamma rays," *Applied Physics Letters*, vol. 97, no. 15, 2010.

[22] PLAUTZ, T. E. A., "200 mev proton radiography studies with a hand phantom using a prototype proton ct scanner.," *TRANSACTIONS ON MEDICAL IMAGING*, vol. 33, no. 4, 2014.

[23] POLF, J. C., PETERSON, S., CIANGARU, G., GILLIN, M., and BEDDAR, S., "Prompt gamma-ray emission from biological tissues during proton irradiation: a preliminary study," *Physics in Medicine and Biology*, vol. 54, no. 3, p. 731, 2009.

[24] POLF, J. C., PETERSON, S., MCCLESKEY, M., ROEDER, B. T., SPIRIDON, A., BEDDAR, S., and TRACHE, L., "Measurement and calculation of characteristic prompt gamma ray spectra emitted during proton irradiation," *Physics in Medicine and Biology*, vol. 54, no. 22, p. N519, 2009.

[25] PROSPER, E., ABEBE, O., and OGRI, U., "Characterization of cerium-doped lanthanum bromide scintillation detector," *Lat. Am. J. Phys. Educ*, vol. 6, no. 1, 2012.

[26] SADROZINSKI, H.-W., BASHKIROV, V., BRUZZI, M., JOHNSON, L., KEENEY, B., ROSS, G., SCHULTE, R., SEIDEN, A., SHAHNAZI, K., WILLIAMS, D., and ZHANG, L., "Issues in proton computed tomography," *Nuclear Instruments and Methods in Physics Research Section A: Accelerators, Spectrometers, Detectors and Associated Equipment*, vol. 511, no. 12, pp. 275 – 281, 2003. Proceedings of the 11th International Workshop on Vertex Detectors.

[27] Schulte, R. W., Bashkirov, V., Loss Klock, M. C., Li, T., Wroe, A. J., Evseev, I., Williams, D. C., and Satogata, T., "Density resolution of proton computed tomography," *Medical Physics*, vol. 32, no. 4, pp. 1035–1046, 2005.

[28] Smeets, J., Roellinghoff, F., Prieels, D., Stichelbaut, F., Benilov, A., Busca, P., Fiorini, C., Peloso, R., Basilavecchia, M., Frizzi, T., Dehaes, J. C., and Dubus, A., "Prompt gamma imaging with a slit camera for real-time range control in proton therapy," *Physics in Medicine and Biology*, vol. 57, no. 11, p. 3371, 2012.

[29] Studenski, M. and Xiao, Y., "Proton therapy dosimetry using positron emission tomography," *World J Radiol*, vol. 2, no. 4, pp. 135–42, 2010.

[30] Yang, M., Zhu, X. R., Park, P. C., Titt, U., Mohan, R., Virshup, G., Clayton, J. E., and Dong, L., "Comprehensive analysis of proton range uncertainties related to patient stopping-power-ratio estimation using the stoichiometric calibration," *Physics in Medicine and Biology*, vol. 57, no. 13, p. 4095, 2012.

[31] Ziegler, J. F., "Srim tables," tech. rep., SRIM, (2013).

VITA

Jessica Saunders was born and raised in suburban Chicago, Illinois. She graduated from Valparaiso University with a Bachelor's of Science degree in Biochemistry in 2007. Following graduation, she participated in protein-protein interaction studies at Argonne National Laboratory and later worked on Hepatitis C Virus entry and egress research at the University of Chicago. After her commissioning in the U.S. Navy as a Radiation Health Officer in September 2011, she was stationed at Walter Reed National Medical Center Bethesda, MD. There she worked with the medical physics team to support the radiology and nuclear medicine departments. She initiated her M.S. in medical physics at Georgia Institute of Technology in 2012 and continued on to pursue her Ph.D in nuclear engineering.